Publication Year	2024
Acceptance in OA@INAF	2024-08-28T14:36:31Z
Title	þÿ F a r a d a y T o m o g r a p h y w i t h C H I M E : T h e T a d p o l e F e a t u
Authors	Mohammed, Nasser; Ordog, Anna; Booth, Rebecca A.; BRACCO, Andrea; Brown, Jo-Anne C.; et al.
DOI	10.3847/1538-4357/ad5099
Handle	http://hdl.handle.net/20.500.12386/35300
Journal	THE ASTROPHYSICAL JOURNAL
Number	971

The Astrophysical Journal, 971:100 (20pp), 2024 August 10 https://doi.org/10.3847/1538-4357/ad5099
© 2024. The Author(s). Published by the American Astronomical Society.
OPEN ACCESS

Faraday Tomography with CHIME: The "Tadpole" Feature G137+7

Nasser Mohammed[1,2], Anna Ordog[1,2], Rebecca A. Booth[3], Andrea Bracco[4,5], Jo-Anne C. Brown[3], Ettore Carretti[6], John M. Dickey[7], Simon Foreman[8], Mark Halpern[9], Marijke Haverkorn[10], Alex S. Hill[1,2], Gary Hinshaw[11], Joseph W. Kania[12,13], Roland Kothes[2], T. L. Landecker[2], Joshua MacEachern[9], Kiyoshi W. Masui[14,15], Aimee Menard[1,2], Ryan R. Ransom[2,16], Wolfgang Reich[17], Patricia Reich[17], J. Richard Shaw[9], Seth R. Siegel[18,19,20], Mehrnoosh Tahani[21], Alec J. M. Thomson[22], Tristan Pinsonneault-Marotte[9], Haochen Wang[14,15], Jennifer L. West[2], Maik Wolleben[23], and Dallas Wulf[19,20]
CHIME and GMIMS Collaborations

[1] Department of Computer Science, Math, Physics, & Statistics, University of British Columbia, Okanagan Campus, Kelowna, BC V1V 1V7, Canada; nmohamme@student.ubc.ca
[2] Dominion Radio Astrophysical Observatory, Herzberg Research Centre for Astronomy and Astrophysics, National Research Council Canada, PO Box 248, Penticton, BC V2A 6J9, Canada; anna.ordog@ubc.ca
[3] Department of Physics and Astronomy, University of Calgary, 2500 University Drive NW, Calgary, Alberta, T2N 1N4, Canada
[4] INAF—Osservatorio Astrofisico di Arcetri, Largo E. Fermi 5, 50125 Firenze, Italy
[5] Laboratoire de Physique de l'Ecole Normale Supérieure, ENS, Université PSL, CNRS, Sorbonne Université, Université de Paris, F-75005 Paris, France
[6] INAF-Istituto di Radioastronomia, Via Gobetti 101, 40129 Bologna, Italy
[7] School of Natural Sciences, University of Tasmania, Hobart, Tas 7000 Australia
[8] Department of Physics, Arizona State University, Tempe, AZ 85287, USA
[9] Department of Physics and Astronomy, University of British Columbia, 6224 Agricultural Road, Vancouver, BC V6T 1Z1, Canada
[10] Department of Astrophysics/IMAPP, Radboud University, PO Box 9010, 6500 GL Nijmegen, The Netherlands
[11] UBC Vancouver Department of Physics and Astronomy, 6224 Agricultural Rd, Vancouver BC V6T 1Z1, Canada
[12] Department of Physics and Astronomy, West Virginia University, P.O. Box 6315, Morgantown, WV 26506, USA
[13] Center for Gravitational Waves and Cosmology, West Virginia University, Chestnut Ridge Research Building, Morgantown, WV 26505, USA
[14] MIT Kavli Institute for Astrophysics and Space Research, Massachusetts Institute of Technology, 77 Massachusetts Avenue, Cambridge, MA 02139, USA
[15] Department of Physics, Massachusetts Institute of Technology, 77 Massachusetts Avenue, Cambridge, MA 02139, USA
[16] Department of Physics and Astronomy, Okanagan College, Kelowna, BC V1Y 4X8, Canada
[17] Max-Planck-Institut für Radioastronomie, Auf dem Hügel 69, 53121 Bonn, Germany
[18] Perimeter Institute for Theoretical Physics, 31 Caroline Street N, Waterloo, ON N25 2YL, Canada
[19] Department of Physics, McGill University, 3600 rue University, Montréal, QC H3A 2T8, Canada
[20] Trottier Space Institute, McGill University, 3550 rue University, Montréal, QC H3A 2A7, Canada
[21] Banting and KIPAC Fellowships: Kavli Institute for Particle Astrophysics & Cosmology (KIPAC), Stanford University, Stanford, CA 94305, USA
[22] ATNF, CSIRO Space & Astronomy, Bentley, WA, Australia
[23] Skaha Remote Sensing Ltd., 3165 Juniper Drive, Naramata, BC V0H 1N0, Canada
Received 2024 January 16; revised 2024 May 24; accepted 2024 May 24; published 2024 August 8

Abstract

A direct consequence of Faraday rotation is that the polarized radio sky does not resemble the total intensity sky at long wavelengths. We analyze G137+7, which is undetectable in total intensity but appears as a depolarization feature. We use the first polarization maps from the Canadian Hydrogen Intensity Mapping Experiment. Our 400–729 MHz bandwidth and angular resolution, 17′–30′, allow us to use Faraday synthesis to analyze the polarization structure. In polarized intensity and polarization angle maps, we find a *tail* extending 10° from the *head* and designate the combined object, the *tadpole*. Similar polarization angles, distinct from the background, indicate that the head and tail are physically associated. The head appears as a depolarized ring in single channels, but wideband observations show that it is a Faraday rotation feature. Our investigations of H I and Hα find no connections to the tadpole. The tail suggests motion of either the gas or an ionizing star through the interstellar medium; the B2(e) star HD 20336 is a candidate. While the head features a coherent, ~ -8 rad m^{-2} Faraday depth, Faraday synthesis also identifies multiple components in both the head and tail. We verify the locations of the components in the spectra using *QU* fitting. Our results show that approximately octave-bandwidth Faraday rotation observations at $\sim$600 MHz are sensitive to low-density ionized or partially ionized gas, which is undetectable in other tracers.

Unified Astronomy Thesaurus concepts: Interstellar medium (847); Interstellar magnetic fields (845); Stellar-interstellar interactions (1576); Radio astronomy (1338); Interstellar dust (836); Interstellar clouds (834); Warm ionized medium (1788); Polarimetry (1278); Proper motions (1295); Radio interferometry (1346)

1. Introduction

Investigations of the Galactic interstellar medium (ISM) have revealed the pervasive presence of magnetic fields and ionized gas (Ferrière 2001). Observations of radio polarization can probe various scales and phases of the ISM, revealing crucial information about the interplay of magnetic fields with other

Original content from this work may be used under the terms of the Creative Commons Attribution 4.0 licence. Any further distribution of this work must maintain attribution to the author(s) and the title of the work, journal citation and DOI.

energy sources. Deriving the three-dimensional configuration of the magnetic field from polarization data can be challenging; nevertheless, recent observations have enabled progress toward a much clearer picture of the evolution of the ISM and the formation of clouds and stars (e.g., Tahani et al. 2022a, 2022b).

At wavelengths of ∼1–100 cm, polarized radiation largely arises from synchrotron emission generated by cosmic-ray electrons as they spiral around magnetic fields. Polarized radiation beyond the Earth's atmosphere was first detected by Westerhout et al. (1962) and Wielebinski et al. (1962) and then extensively mapped by Brouw & Spoelstra (1976). Recent surveys of this polarized radiation have Nyquist-sampled wide areas of the sky in different frequency ranges (Wolleben et al. 2019, 2021; Carretti et al. 2019).

Linearly polarized electromagnetic waves undergo Faraday rotation as they propagate through a magneto-ionic medium. The resulting change in polarization angle informs us of electron density and magnetic field strength and direction. Exploiting this effect, polarized emission from extragalactic sources propagating through the Galaxy has been used to measure the two-dimensional distribution of magnetic fields in the Milky Way and nearby galaxies averaged along the line of sight (Brown et al. 2003; Taylor et al. 2009; Mao et al. 2012a; Ordog et al. 2017; Tahani et al. 2018; Van Eck et al. 2021; Hutschenreuter et al. 2022; Thomson et al. 2023). The Faraday rotation of the emission of the Galaxy itself is an especially powerful probe of the diffuse ISM because the emitting cosmic rays and the Faraday-rotating thermal gas are mixed, where these emission regions illuminate different Faraday-rotating regions along the line of sight (e.g., Gaensler et al. 2001; Mao et al. 2012b; Van Eck et al. 2017).

Faraday rotation probes the convolution of ionized gas density and the line-of-sight magnetic field; therefore, it is sensitive to two distinct components of the ISM. The majority of the ionized gas in the Milky Way ISM is found in the warm ionized medium (WIM), traced by Hα emission with an ionization fraction $\gtrsim$90% based on observations of the [O I] λ6300 line (Hausen et al. 2002). However, particularly at low frequencies $\lesssim$1 GHz, Faraday rotation is sensitive to very small columns of free electrons and might trace a warm partially ionized medium (Heiles & Haverkorn 2012) or the low (few percent; Wolfire et al. 2003; Jenkins 2013) ionization in the warm neutral medium (Foster et al. 2013; Van Eck et al. 2017; Bracco et al. 2022). In fact, low-frequency Faraday rotation observations may not be sensitive to the traditional WIM (Haffner et al. 2009) at all because the electron density there is high enough to cause depolarization (DP), even with weak magnetic fields (Van Eck et al. 2017).

Burn (1966) established the formalism for extracting three-dimensional information on the diffuse magneto-ionized ISM with mixed synchrotron emission and Faraday rotation. However, the technique requires data over a wide range of wavelength squared (λ^2), which became feasible only recently with the advent of radio telescopes equipped with wideband receivers and modern digital signal processors (Brentjens & de Bruyn 2005; Heald 2009). Useful λ^2 coverage typically implies low frequencies and wide bandwidths (ideally octave or more). The use of Faraday synthesis,[24] a form of Faraday tomography (Takahashi 2023), enables studies of the large-scale structure of the magnetic field (Dickey et al. 2019, 2022; Erceg et al. 2022), and also of individual objects and small regions (e.g., Schnitzeler et al. 2007; Van Eck et al. 2017, 2019; Thomson et al. 2019, 2021). Direct modeling of the spectra of Stokes parameters Q and U (*QU fitting*) has proven able to detect multiple Faraday depth components in Faraday complex spectra more reliably than Faraday synthesis, but with the drawbacks of needing considerably longer computational time for each line of sight and requiring us to assume a Faraday rotation model (Farnsworth et al. 2011; O'Sullivan et al. 2012; Ideguchi et al. 2014; Sun et al. 2015). In practice, one often uses Faraday synthesis to inform the selection of models for QU fitting.

Here, we study a region, G137+7, first discovered by Berkhuijsen et al. (1964) in a polarization survey of the northern sky at 610MHz as a ring of low polarization, 2° in diameter, centered on $\ell = +137°$, $b = +7°$. It lies in the so-called Fan region, an area otherwise bright in polarized intensity and uniform in polarization angle at 408 MHz (Verschuur 1968). Verschuur (1969) associated it with the star HD 20336 (distance 246 ± 20 pc; Gaia Collaboration et al. 2023), suggesting that the B2(e) star had tunneled its way through a cloud of neutral hydrogen, disrupting it and ionizing a portion of the hydrogen gas. Haverkorn et al. (2003) detected this polarized circular object at 350 MHz, but considered HD 20336 an unlikely progenitor for the feature on account of the star's high proper motion of 18 mas yr^{-1} being too large to maintain a circular Strömgren sphere. Instead, they suggest that the structure would be elongated in the direction opposite to the motion of the star. Iacobelli et al. (2013) used 150 MHz Faraday synthesis to place the object at a distance of ∼100 pc, possibly in the wall of the Local Bubble. The lack of a detectable H II region led to the suggestion that the source of ionization might be an unidentified white dwarf. In this paper, we present observations that reveal a tail-like prominence extending approximately 10° from a prominent circular region of Faraday rotation, coincident with the structure studied by earlier authors. This head-tail structure has led us to name G137+7 the *tadpole*.

The outline of this paper is as follows. In Section 2, we review Faraday rotation and Faraday synthesis. In Section 3, we describe the Canadian Hydrogen Intensity Mapping Experiment (CHIME) data (Section 3.2), the Dominion Radio Astrophysical Observatory (DRAO) Synthesis Telescope (ST) data (Section 3.3), and published data sets to which we compare the CHIME maps (Section 3.4). We present the observed features of the tadpole in Section 4 and discuss its origin in Section 5. We summarize the paper in Section 6. In Appendix A, we present simulations of the impact of marginally resolved Faraday complexity on Faraday synthesis observations. In Appendix B, we present our QU-fitting results.

2. Faraday Rotation and Faraday Synthesis

If a polarized photon is emitted with an intrinsic polarization angle χ_0, the polarization angle we measure at wavelength λ after this signal has been Faraday rotated by the Galactic ISM is

$$\chi = \chi_0 + \phi \cdot \lambda^2. \tag{1}$$

The Faraday depth, ϕ, is defined as (Ferrière et al. 2021)

$$\frac{\phi}{(\mathrm{rad\ m^{-2}})} = 0.81 \int_{\mathrm{emission}}^{\mathrm{observer}} \frac{n_e}{\mathrm{cm^{-3}}} \frac{\boldsymbol{B}}{\mu\mathrm{G}} \cdot \frac{d\boldsymbol{l}}{\mathrm{pc}}, \tag{2}$$

[24] We mostly adopt the terminology described in Table 1 of Sun et al. (2015): "Faraday depth," "Faraday spectrum," "Faraday synthesis" (Brentjens & de Bruyn 2005), "RMSF," "Faraday clean" (Heald 2009), and "3D Faraday synthesis" (Bell & Enßlin 2012).

where n_e is the electron density of the ISM, and we are projecting the magnetic field, $\boldsymbol{B}$, along our line of sight, $\boldsymbol{dl}$. There is a Fourier transform-like relationship between the observable complex polarization[25] $\tilde{P}(\lambda^2) = Q + iU$ and the Faraday spectrum $\tilde{F}(\phi)$, which is recoverable through a process known as Faraday synthesis (Burn 1966; Brentjens & de Bruyn 2005). The polarized intensity at each Faraday depth is $p(\phi)I \equiv \sqrt{Q(\phi)^2 + U(\phi)^2}$, where $p(\phi)$ is the fractional polarization and I is the total intensity. The Faraday spectrum is the spectrum of polarized intensity as a function of Faraday depth for each line of sight. A weighting function $W(\lambda^2)$ introduces a rotation measure spread function (RMSF), $\tilde{R}(\phi)$, the Fourier transform of $W(\lambda^2)$. Gaps in $W(\lambda^2)$ result in sidelobes in $\tilde{R}(\phi)$. Utilizing polarization data over a wide range of wavelengths allows the creation of a (complex) Faraday depth cube of $\tilde{F}(\ell, b, \phi)$ for Galactic coordinates (ℓ, b).

The Faraday depth resolution, measured as the FWHM of the main lobe of $R(\phi) = |\tilde{R}(\phi)|$, can be approximated as (Schnitzeler et al. 2009)

$$\delta\phi \approx \frac{3.8}{\lambda^2_{\rm max} - \lambda^2_{\rm min}} \tag{3}$$

for reference wavelength λ_0 (the wavelength to which the polarization angles are derotated; Brentjens & de Bruyn 2005, Equations (25)–(26)) set to the average λ^2 in the band (as we do in this paper). The largest-scale feature in Faraday depth space that is not depolarized is (Brentjens & de Bruyn 2005)

$$\phi_{\rm max-scale} \approx \frac{\pi}{\lambda^2_{\rm min}}. \tag{4}$$

Rudnick & Cotton (2023) argue that setting $\lambda_0 = 0$ recovers additional information and modifies Equations (3) and (4), but we use traditional Faraday synthesis in this work.

3. Data and Instruments

3.1. CHIME and Global Magneto-ionic Medium Survey Surveys

This work is a part of the Global Magneto-Ionic Medium Survey (GMIMS), a collaboration using telescopes in the Northern and Southern hemispheres to obtain all-sky diffuse polarization maps with frequency coverage and resolution designed to, in combination, be sensitive to large Faraday depth scales ($\phi_{\rm max-scale} \sim 100\,{\rm rad\,m^{-2}}$) with fine sensitivity to small Faraday depth structures ($\delta\phi \sim 10\,{\rm rad\,m^{-2}}$). This requires frequency coverage from ∼300–1800 MHz with thousands of frequency channels. GMIMS also requires sensitivity to all spatial scales above the resolution limit, which prefers the use of single-antenna telescopes. GMIMS low-band south (300–480 MHz using the Murriyang Telescope at the Parkes Observatory; Wolleben et al. 2019) and high-band north (1280–1750 MHz using the John A. Galt Telescope at DRAO; Wolleben et al. 2021) data products are public. This work uses prerelease data from the low-band north survey using CHIME at DRAO. The CHIME instrument is described in detail by CHIME Collaboration (2022). The CHIME data pipeline, including RFI excision, complex gain calibration, averaging over redundant baselines, and stacking over sidereal days, is described in CHIME Collaboration (2023). The CHIME/GMIMS low-band north polarization data set will be described in detail elsewhere (CHIME & GMIMS Collaborations 2024, in preparation, hereafter "CHIME/GMIMS survey paper"). We present a brief overview of the data and processing steps here.

3.2. CHIME/GMIMS Low-band North

We use all-sky diffuse polarization data from CHIME for polarization observations of the tadpole feature and as the basis for Faraday synthesis of the region. CHIME consists of four stationary parallel cylindrical reflectors, measuring 1024 frequency channels across its range of 400–800 MHz. Oriented north–south, each $100 \times 20{\rm m}^2$ cylinder has 256 dual-polarization linear feeds (X and Y) spaced every 30 cm along the central 78m of the focal line. CHIME observes the entire meridian at any given moment with baselines from 0.3–78 m, mapping the northern sky every sidereal day. This gives the telescope the ability to collect data at a range of angular scales, resulting in an effective angular resolution of approximately 30′ at 400 MHz (Masui et al. 2019). We exclude autocorrelations of feeds with themselves. As an interferometer, CHIME is missing the very largest scales corresponding to baselines <0.3m or angular scales ≳50°. A future survey with the DRAO 15 m Telescope (A. Ordog et al. 2024, in preparation) will provide the largest scales for the final GMIMS low-band north data product.

We generate full sky maps known as *ringmaps* by performing a one-dimensional Fourier transform on ∼21 s samples of the visibilities in the north–south direction along the meridian. As the sky passes through the primary beam, we sample the full range of right ascension values with these one-dimensional images each sidereal day, which we combine to produce the full map. We employ stacked ringmaps, using nighttime-only visibilities from 102 nights of data collected from 2019 January to November. The CHIME beam profile, which is declination dependent and somewhat different in the XX and YY polarizations due to the cylindrical and stationary design of the telescope, is one of our largest uncertainties; for this reason, in this paper, we report CHIME data in jansky per beam rather than brightness temperature units and confine ourselves to a relatively small declination range at a low zenith angle (⩽21°) where the beam is nearly constant.

The ringmaps we use do not have beam deconvolution applied. There are small artifacts in the image, resulting from this, which we describe in Section 4.5; however, their presence is not detrimental to studying structures on the scale of several degrees, such as the tadpole. In this analysis, we use the 400–729 MHz subset of the full CHIME band, as the highest frequencies are contaminated by aliasing, which makes the maps unreliable in the region of interest.

3.2.1. Polarization Angle Calibration

To calibrate CHIME polarization angles $\chi \equiv 0.5\tan^{-1}(U/Q)$ (calculated using the full $\pm\pi$ range accounting for the signs of U and Q), we rely only on CHIME co- and cross-polar data products and two key assumptions: that Stokes $V = 0$ (averaged over right ascension at every declination), and that the gain difference ΔG between the X and Y polarizations is small. Because of the declination-dependent beam properties of CHIME, we calibrate each declination in the raw maps using data within a 1° strip, centered on that declination, and covering

[25] We use a tilde to indicate complex values.

the full right ascension range. We focus on the narrow declination range around G137+7, $+60° \lesssim \delta \lesssim 70°$. This covers zenith angles 11°–21°, a region in which the CHIME beam model is best (CHIME Collaboration 2022, 2023).

We represent the co-polar power from the orthogonal feeds as $X'_C X'_C$ (east–west feeds) and $Y'_C Y'_C$ (north–south feeds) and the (complex) cross-polar term as $X'_C Y'_C$. We use the stacked $X'_C X'_C$, $Y'_C Y'_C$, and $X'_C Y'_C$ ringmaps. Here, X_C and Y_C refer to the CHIME coordinate system (CHIME Collaboration 2022), in which the naming of the variables X and Y is interchanged from the IAU convention (IAU 1973). (The spherical CHIME cosmology X_C and Y_C coordinate system used here is also different from the Cartesian CHIME/Fast Radio Burst (FRB) coordinate system; CHIME/FRB Collaboration 2021.) The prime notation indicates detected values after passing through the full CHIME system, so the observed Stokes vector is

$$\mathcal{S}' \equiv \begin{pmatrix} I' \\ Q' \\ U' \\ V' \end{pmatrix} = \begin{pmatrix} 0.5(Y'_C Y'_C + X'_C X'_C) \\ 0.5(Y'_C Y'_C - X'_C X'_C) \\ \mathrm{Re}(Y'_C X'_C) \\ -\mathrm{Im}(Y'_C X'_C) \end{pmatrix} = M\mathcal{S} \tag{5}$$

for Müller matrix M and true sky Stokes vector $\mathcal{S}$. This follows the IAU convention with linear position angles increasing counterclockwise when looking at the source (IAU 1973).

Using linear feeds to measure Stokes Q requires the careful subtraction of two large numbers (the autocorrelations), whereas Stokes U involves measuring the small cross-correlation. For calibration of Q and U, we perform data-based estimates of the cross terms in M following Heiles (2002). First, we assume that the difference in gains G_X and G_Y is small enough to approximate $\Delta G = (G_Y - G_X)/(G_Y + G_X) \ll 1$. We calculate the average ΔG at each declination and frequency from a linear regression of $Y'_C Y'_C$ as a function of $X'_C X'_C$, using data within a 1° decl. bin (overlapping bins centered on each declination) and covering the full 24 hr R.A. range. Over the declination range of the tadpole region (45°–80°) and the frequencies used in this analysis, we find the mean and median of ΔG to be −0.43 and −0.38, respectively, with 73% of declinations and unflagged frequencies having $|\Delta G| < 0.5$. Although this does not strictly satisfy $\Delta G \ll 1$, it is sufficiently small, so the defined ΔG term dominates over second-order corrections. The gain difference is dominated by differences in the beam solid angle between the two polarizations due to the asymmetric design of the CHIME telescope. We then apply this declination- and frequency-dependent ΔG to correct for leakage between Stokes I and Q,

$$Q = \frac{Q' - I'\Delta G/2}{1 - (\Delta G/2)^2} \tag{6}$$

Stokes U and V are measured from the cross-correlation products. We assume that $\langle V \rangle = 0$ from the sky in diffuse emission because synchrotron emission in low-density astrophysical environments does not produce circular polarization. Leakage between V and U arises from phase offsets. We measure a mean phase shift $\langle \psi \rangle(\delta, \nu)$ at each declination and frequency, assuming that $\langle V \rangle = 0$ and calculate

$$U = U' \cos\langle \psi \rangle + V' \sin\langle \psi \rangle. \tag{7}$$

The $\langle V \rangle = 0$ assumption leads to high-quality fits even in FRB observations, where the assumption has less clear physical justification than in the diffuse polarized emission we investigate (Mckinven et al. 2023). We find that the phase shift is linear in frequency, consistent with a cable delay $\tau = \langle \psi \rangle / 2\pi\nu \sim 1$ ns for the diffuse emission, as Mckinven et al. (2021, their Appendix A) found in CHIME/FRB data.

In Figure 1, we compare the calibrated data to the Dwingeloo telescope survey at 610 MHz in the Fan region (Brouw & Spoelstra 1976). There is a strong correlation between Dwingeloo U and CHIME U and Dwingeloo Q and CHIME Q in those directions for which there is Dwingeloo data, with correlation coefficient R values of 0.91 for $U - U$ and 0.89 for $Q - Q$ comparisons. This is a significant improvement from the uncalibrated correlation coefficients of 0.76 and 0.59, respectively. We find a remaining leakage of up to 20% in Stokes Q based on unresolved point source measurements. Using the mean orthogonal distance between each point and the fitted line, we find that noise from CHIME and Dwingeloo data describes ≈70% of the scatter in Figure 1. The polarization angle correlation, also shown in Figure 1, is also improved through calibration, and most outliers are points with low polarized intensity (yellow dots), where the uncertainty in derived χ is high.

We show the resulting CHIME Q and U maps, with the $\chi = 0$ reference axis rotated to the north Galactic pole, in Figure 2. While Stokes I to Q leakage does exist in our data, the tadpole structure cannot simply be the result of leakage. Although there is total intensity emission over the entire Fan region, including the tadpole, this emission is featureless on small scales and thus cannot produce spurious polarization matching the tadpole in morphology. Furthermore, the tadpole cannot be the product of Stokes I emission originating at large angular distances (such as the Galactic plane) and seen in far sidelobes. While the far sidelobes have poor polarization properties, their polarization averages to low values over sizable areas. Moreover, with linear feeds, leakage from I is primarily into Q, not U (in the native equatorial coordinates of CHIME), but the tadpole is already evident in Stokes U in equatorial coordinates (not shown).

The slopes of $U - U$ and $Q - Q$ inform the calculation of the beam solid angle in converting jansky per beam to brightness temperature units. From these slopes, we deduce that 1 Jy beam^{-1} corresponds to 1.79K. The effective area of CHIME is, therefore, 4900 m^2 at 610 MHz, confirming that, in our application, CHIME acts like a large single-antenna telescope. This paper focuses on Faraday rotation effects, meaning that the primary data product is the polarization angle and its variation with frequency. Absolute calibration of the amplitude scale is thus of minor significance for the present work, and we report intensities in units of jansky per beam, leaving a more careful conversion to temperature units for the CHIME/GMIMS survey paper.

The CHIME observations were made in 2019, at solar minimum. Only nighttime data were used. The observations were not corrected for Faraday rotation in the ionosphere, but we expect the effect to be smaller than 1 rad m^{-2}, with an rms value of 0.3 rad m^{-2}. The result is a small decrease in polarized intensity since we averaged together observations from different nights.

3.2.2. Faraday Synthesis on CHIME Data

We apply Faraday synthesis to the Stokes Q and U cubes from the calibrated CHIME polarization data in Galactic coordinates using `RMTools_3D` in the `RM-Tools` software

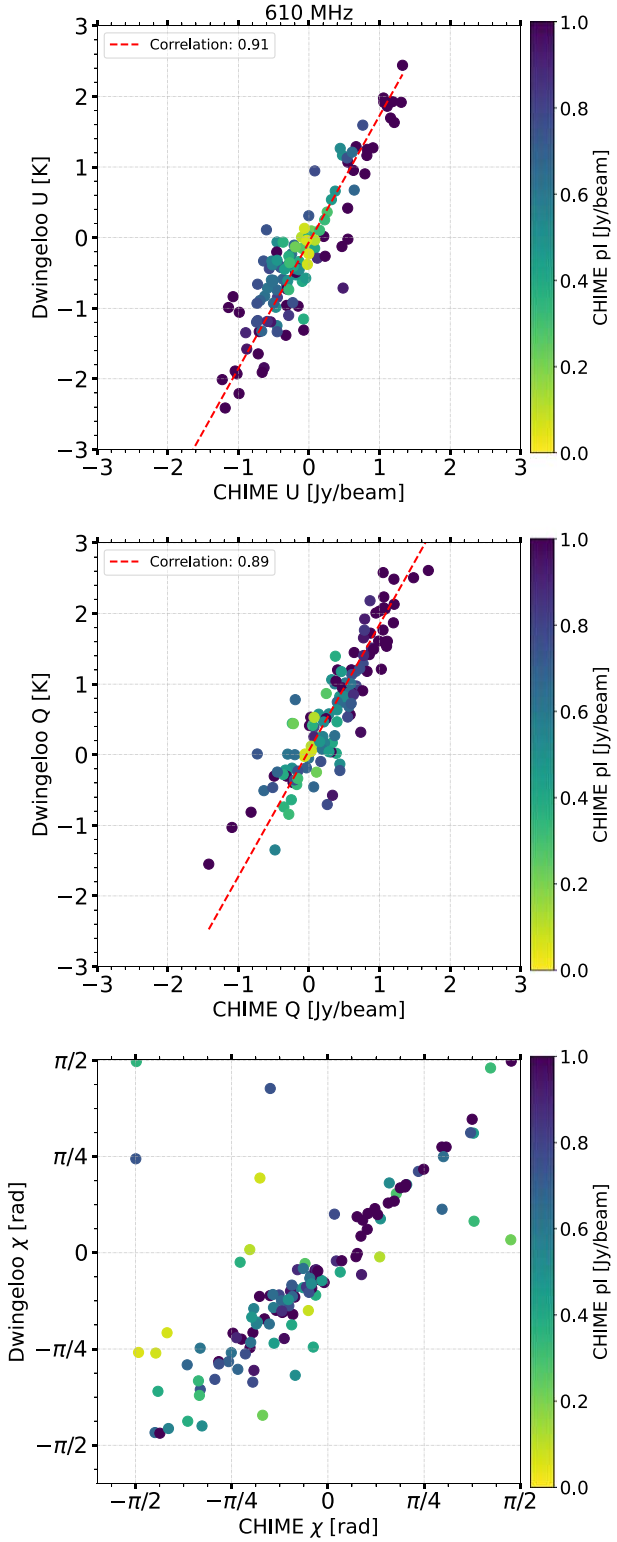

Figure 1. Comparisons between the Dwingeloo (Brouw & Spoelstra 1976) absolutely calibrated Q and U observations in the Fan region ($120° \lesssim \ell \lesssim 180°$, $-2° \lesssim b \lesssim 30°$) at 610 MHz and CHIME 614 MHz. All data points show a Dwingeloo pointing and the median of corresponding CHIME data within the Dwingeloo beam. The color bar is the CHIME polarized intensity for these points. For Stokes Q and U, the Dwingeloo data are shown in brightness temperature units and CHIME data in jansky per beam.

package (Purcell et al. 2020). We show images of the main products of Faraday synthesis in Figure 3, and the magnitude of the RMSF along with frequency and λ^2 coverage in Figure 4.

For each pixel in the maps, we calculate the dirty Faraday spectrum out to ± 200 rad m^{-2} sampled every 0.5 rad m^{-2}. This extent in ϕ is sufficient to include the major structures without being dominated by sidelobes. We do not convolve the CHIME data to a common resolution prior to Faraday synthesis, as this may be unreliable due to uncertainties in the synthesized beam shape. With the resolution only varying between $\sim 30'$ (at 400 MHz) and $\sim 17'$ (at 729 MHz), structures on the scale of the tadpole (several degrees) are largely unaffected.

The 400–729 MHz frequency coverage yields $\delta\phi = 9.7$ rad m^{-2} and $\phi_{\rm max-scale} = 19$ rad m^{-2}. With $\delta\phi < \phi_{\rm max-scale}$, we expect CHIME data to resolve somewhat extended Faraday depth structures. For all lines of sight in the tadpole region (Section 4.2), we apply the `RM-Tools` implementation of the `RM-CLEAN` algorithm (Heald 2009) to reduce the sidelobes in the spectra, using a `CLEAN` threshold of 0.2 Jy beam^{-1} based on an estimate of the noise in the dirty spectra. We present CLEANed spectra in Section 4.2 below.

Using the `rmtools_peakfitcube` algorithm in `RM-Tools`, we obtain the peak Faraday depth and its associated error for every spectrum along all lines of sight. The resulting map is shown in Figure 3(b). We use peak Faraday depths rather than a first moment (Dickey et al. 2019) to focus on the Faraday depth of the brightest feature in each line of sight rather than a weighted mean Faraday depth in Faraday complex regions.

We show the integrated polarized intensity across the Faraday depth spectra as a zero moment map in Figure 3(a). A polarization angle map derotated to χ_0 by the peak Faraday depth at each pixel is shown in Figure 3(c).

3.3. DRAO Synthesis Telescope Observations

We use new and previously published polarized continuum and H I observations from the DRAO ST (Landecker et al. 2000). The ST continuum observations combine four 7.5 MHz-wide frequency channels within a 35 MHz bandpass centered on 1420.4 MHz to measure Stokes Q and U using dual circular polarization feeds. The ST H I observations are produced by a 256-channel spectrometer with a velocity range between 211 and 1.32 km s^{-1} spectral resolution. Existing observations come from the Canadian Galactic plane survey (CGPS; Taylor et al. 2003; Landecker et al. 2010), covering Galactic latitudes of $-3° < b < +5°$. We use a variety of ST fields observed and calibrated in the same manner as CGPS fields for a number of projects, some previously published (West et al. 2007; Kothes et al. 2014), and some unpublished, covering $+5° < b < +12°$.

In all ST polarized continuum observations, single-channel 1410 MHz polarization observations from the Effelsberg Medium-Latitude Survey (EMLS; Uyanıker et al. 1998, 1999; Reich et al. 2004, P. Reich et al. 2024, in preparation.) provide single-antenna information. The EMLS data are based on Effelsberg 100 m Telescope observations from latitude $|b| < 20°$, observed mostly in blocks $7° \times 7°$ in size but with many exceptions to avoid strong source complexes at the map boundaries. Emission exceeding the map size is missing and was restored by combining with the northern-sky Galt Telescope survey (Wolleben et al. 2006). We then combine this single-antenna data with the ST 1420 MHz data as follows. First, we mosaicked the ST fields together following Taylor et al. (2003). Then, we convolve the ST data to $10.'4$, slightly larger than the $9.'35$ EMLS resolution. We then subtract the convolved ST data (Stokes Q and U separately) from the EMLS data; the residual is

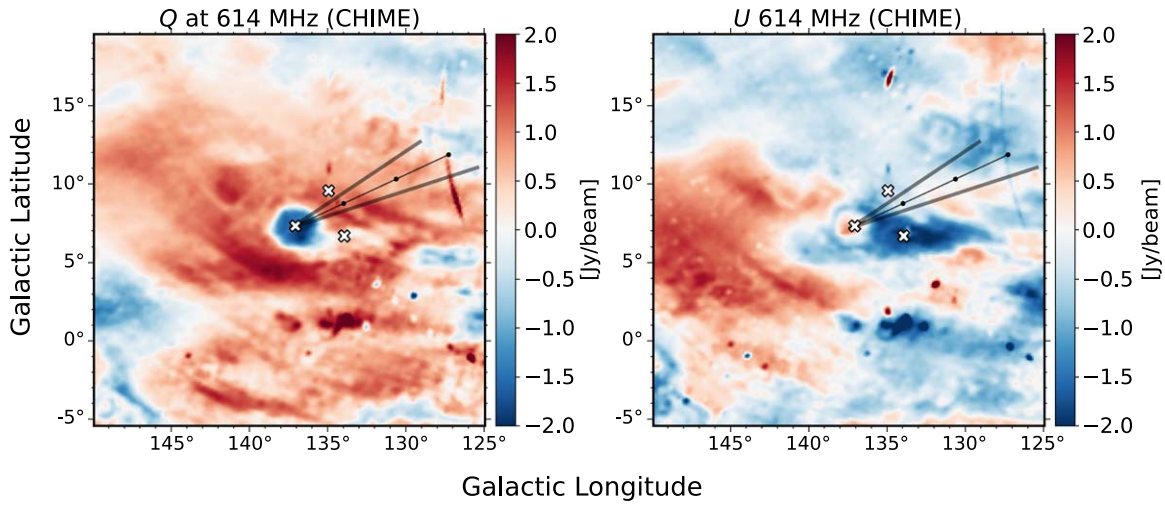

Figure 2. Images of the tadpole region in Stokes Q and U at 614 MHz in Galactic coordinates. The "×" markers indicate the position of B2(e) star HD 20336 (the × near the center of the circular tadpole head) as well as the selected spectra shown in Figure 7. The thin black line represents the LSR-corrected proper motion of HD 20336, projected backward in time over 3 Myr, with each dot representing 1 Myr. The translucent lines represent the error cone, which is dominated by the uncertainty in the LSR correction.

the large-scale structure missed in the ST data (Reich et al. 1990). Finally, we add the residual to the original ST data to produce Q and U images, including scales from $1'$ to the full sky. This technique is somewhat different from that used for the CGPS, where ST+EMLS data were combined in Fourier space (Landecker et al. 2010), but produces very similar results. We refer to this combined data set of interferometric observations from the ST with single-antenna data from the Effelsberg and Galt telescopes as "ST+EMLS," and show the resulting polarized intensity and polarization angles maps for the tadpole region in Figures 5(i) and (j).

In our ST atomic hydrogen observations, we incorporate the HI4PI Survey of H I 21 cm brightness temperature, with an angular resolution of $16\farcm2$, velocity coverage of $\leqslant 600\ \mathrm{km\ s^{-1}}$, and spectral resolution of $1.49\ \mathrm{km\ s^{-1}}$ (HI4PI Collaboration et al. 2016), to provide the majority of the single-antenna information. The fields we incorporated that were previously processed for the CGPS used the DRAO 26 m data to provide short-spacing information on account of HI4PI being unavailable at the time. We process a wider field of view for the H I observations than for the polarized continuum observations—covering Galactic latitudes of $-4° < b < +12°$ and longitudes of $126° < l < 149°$—to highlight typical fluctuations seen across the diffuse neutral medium (see Section 5.1). For each ST field in this region, we determine continuum emission by averaging the H I channels void of 21 cm emission, then subtracting this to isolate only H I emission. We calibrate, merge short-spacing and ST data, and mosaic the H I fields by the same procedure used for the CGPS Taylor et al. (2003). This results in the H I brightness temperature map, which we refer to as "ST+HI4PI."

3.4. Ancillary Data Sources

We use data from the Westerbork Synthesis Radio Telescope (WSRT) at 150 MHz (Bernardi et al. 2009; Iacobelli et al. 2013, provided by M. Iacobelli, 2023, private communication) and 350 MHz (Haverkorn et al. 2003) to supplement discussions of observed DP. We summarize the observing parameters for all four polarization data sets used in this paper in Table 1. The five channels in the 350 MHz data are not sufficient for Faraday synthesis, measuring only the rotation measure $\mathrm{RM} = d\chi/d\lambda^2$. For the 150 MHz data, only post-Faraday synthesis data are available, so we cannot show single-frequency images or perform QU fitting on these data. We show the WSRT polarized intensity and polarization angle maps in Figures 5(a)–(d).

We use the Wisconsin H-Alpha Mapper (WHAM) survey of Hα emission to study ionized hydrogen in the region (Haffner et al. 2003, 2010). WHAM has an angular resolution of 1° and provides a kinematically resolved map of Hα emission within $\approx 100\ \mathrm{km\ s^{-1}}$ of the local standard of rest (LSR) with $12\ \mathrm{km\ s^{-1}}$ spectral resolution.

4. Features of the Tadpole

4.1. Morphology in Single-frequency Images

We show images of the tadpole region in Q and U at 614 MHz in Figure 2, image products derived from Faraday synthesis with CHIME in Figure 3, and pI and χ from the polarization data sets described above, covering 150–1420 MHz, in Figure 5. The tadpole is immediately apparent in the single-channel CHIME Q and U images in Figure 2 with a circular feature we call the head near $(\ell, b) = (137°, +7°)$ and a *tail* extending to the right as far as (127°, +6°), most clearly in U. The structure as a whole strongly resembles the larval stage of amphibians, leading us to nickname it the tadpole. We use the name "G137+7" to refer to the circular region first identified by Verschuur (1968), and the name tadpole to describe the entire feature, including the tail. The head (G137+7) is the feature that has been studied since Verschuur (1968); it is visible in all channels in Figure 5.

At 150 MHz (Figures 5(a) (b)), the head is evident as a large, diffuse structure in pI. There is a circular pattern to the polarization angles, suggesting rapid wrapping through π radians as one moves outward radially from the center of the head.

At 350 MHz (Figures 5(c), (d)), the head appears as a ring in pI (Figure 5(c)). Haverkorn et al. (2003) measured $\mathrm{RM} = -8\ \mathrm{rad\ m^{-2}}$ in the center of the head. At this frequency, the head is also a ring in χ, with approximately two full rotations through π radians in the radial direction. This is consistent with the RM changing from $-8\ \mathrm{rad\ m^{-2}}$ in the center of the head to $0\ \mathrm{rad\ m^{-2}}$ outside the head,

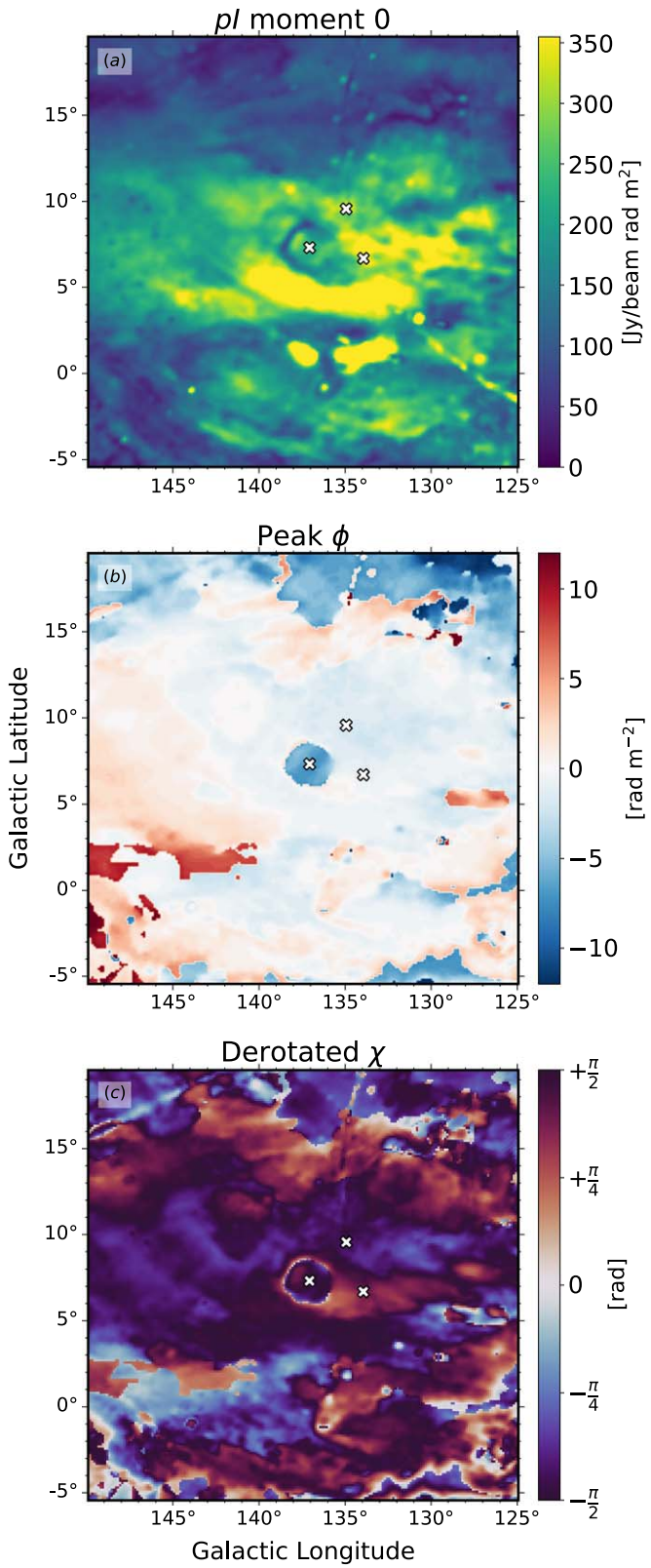

Figure 3. Maps of products of Faraday synthesis generated from the 400–729 MHz channels of CHIME. (a) Moment zero integrated polarized intensity. (b) Faraday depth of highest peaks of the Faraday depth spectra. (c) The derotated polarization angle (i.e., the angle at the point of emission). The "×" markers are as in Figure 2.

which would correspond to an angle change $\Delta\chi = \phi\lambda^2 = 6$ radians. Haverkorn et al. (2003) point out an elongated structure of

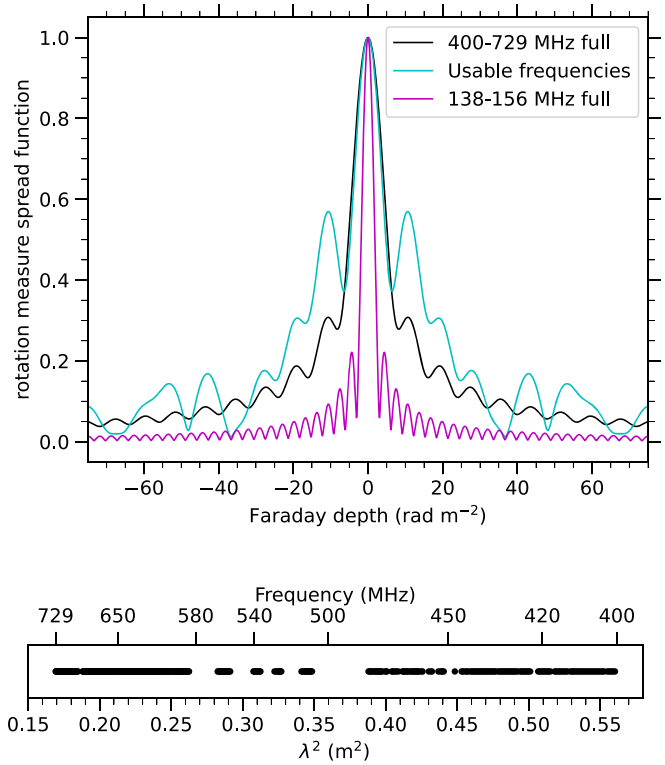

Figure 4. Top: magnitude of the RMSF for the full CHIME frequency range (black lines), the usable CHIME frequency channels (cyan line), and the full WSRT 150 MHz frequency range (magenta line). See Table 1. Bottom: usable CHIME frequencies, $W(\lambda^2)$ (bottom axis) or $W(\nu)$ (top axis). The WSRT RMSF shown here assumes full frequency coverage from 138–156 MHz because we have no record of the missing frequencies.

high *pI* extending northwest, which they say does not necessarily have the same origin as the ring; this is evident in both *pI* (Figure 5(c)) and χ (Figure 5(d)). This appears to be the tail.

At 410 MHz in the CHIME *pI* data, the clearest signature of the head is a narrow ring of *low* polarized intensity, which extends in a nearly complete circle. At 614 MHz, there is a similar ring of low polarized intensity, but only in a semicircle on the left (east) side of the head. This feature is one beam wide, a clear signature of beam DP, with the polarization angle changing within the beam such that there is destructive interference, reducing the polarized intensity (Sokoloff et al. 1998; Gaensler et al. 2001). The same feature is evident in *pI* from the Faraday synthesis products in Figure 3, but it does not stand out as much: by using information at a wide range of λ^2, the Faraday synthesis product is less sensitive to beam DP than single-frequency images. Furthermore, if the depolarized ring arises from beam DP, we would not expect to see it in the ST+EMLS data, due to the significantly smaller beam ($1'$ compared to $30'$). This is, in fact, the case in Figure 5(i): none of the head, the depolarized ring, or the tail is evident in *pI*.

In polarization angle, the 410 MHz CHIME data show a clear wrap through π radians moving radially from the center of the head to outside the ring (Figure 5(f)). The tail of the tadpole stands out clearly, especially as a polarization angle feature in Figure 3(c) and Figures 5(f), (h). The tadpole, both head and tail, is also visible at 1420 MHz in the ST+EMLS polarization angle image (Figure 5(j)), despite not being evident in *pI*. The large-scale structure at 1420 MHz is similar to that observed in CHIME 614 MHz polarization angle (Figure 5(h)), where the χ

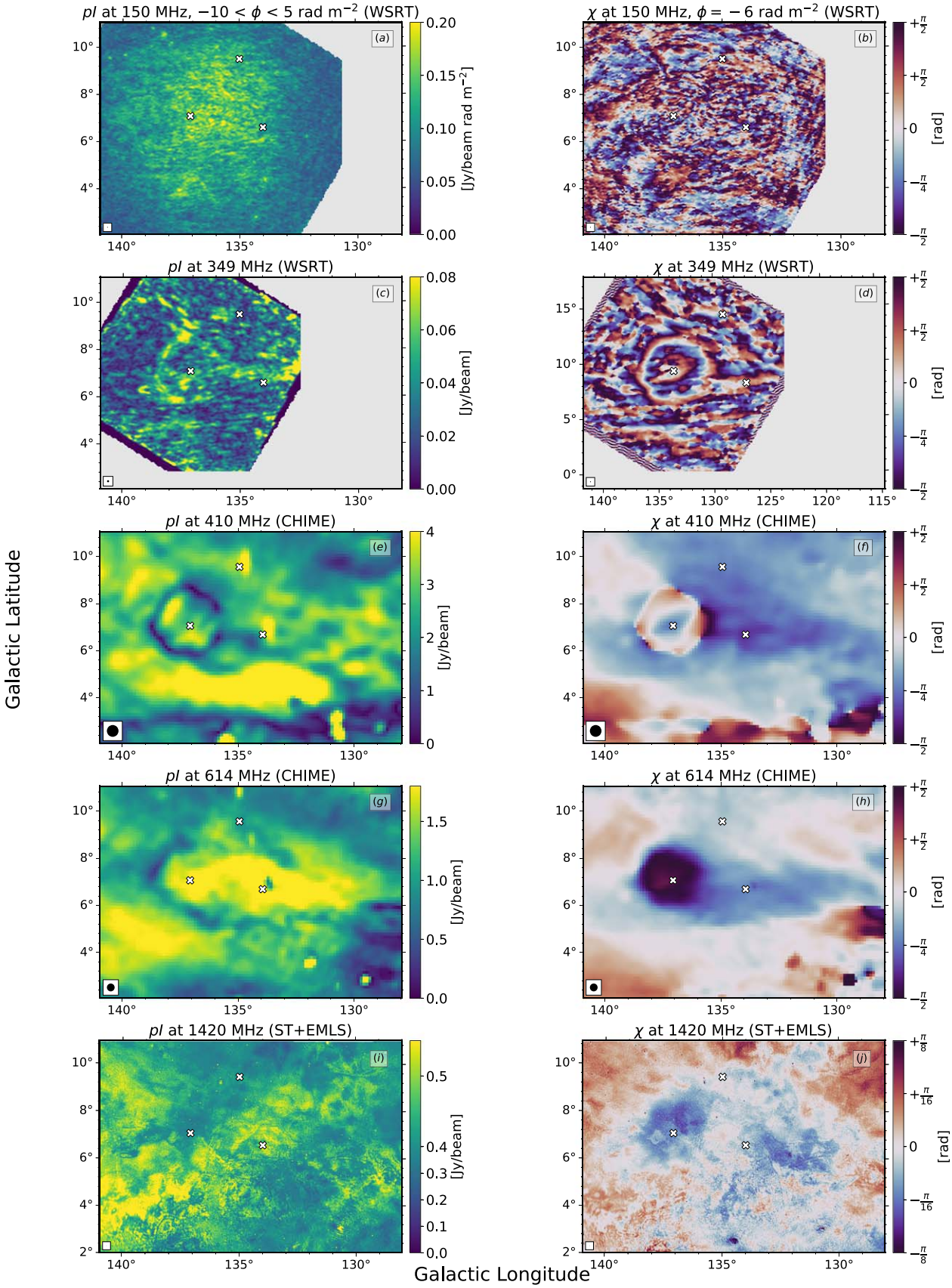

Figure 5. The tadpole depicted in polarized intensity (left) and polarization angle (right). From top to bottom: (a), (b) Bernardi et al. (2009) Faraday synthesis data at frequencies ∼150 MHz with the WSRT at $\phi = -2$ rad m^{-2} (a frequency data cube is unavailable), (c), (d) Haverkorn et al. (2003) single-frequency polarized intensity and polarization angle at 349MHz, CHIME data at (e), (f) 410 MHz and (g), (h) 614 MHz, and (i), (j) 1.4 GHz DRAO ST+EMLS data. "×" markers are as in Figure 2. Beams are shown within each image. Beams for the WSRT and ST+EMLS data are too small to be easily visible (see Table 1).

Table 1
Observing Parameters

	Bernardi et al. (2009), Iacobelli et al. (2013)	Haverkorn et al. (2003)	This Paper	This Paper, Landecker et al. (2010)
Instrument	WSRT	WSRT	CHIME	ST+EMLS
Observed field	$\sim 12° \times 12°$	$\sim 7° \times 7°$	all-sky	Galactic plane plus $20° \times 7°$ extension
Frequencies	138–156 MHz	341–375 MHz	400–729 MHz	1.4 GHz
Channels	2048×9.8 kHz	5×5 MHz	844×390 kHz	1×35 MHz
λ^2 coverage	3.7–4.7 m^2	0.64–0.77 m^2	0.17–0.56 m^2	0.04 m^2
$\delta\phi$ (equation 3)	3.8 rad m^{-2}	29 rad m^{-2}	9.7 rad m^{-2}	n/a
$\phi_{\mathrm{max-scale}}$ (Equation 4)	0.8 rad m^{-2}	n/a	19 rad m^{-2}	n/a
Angular resolution	$2' \times 2.'2$	$5.'0 \times 5.'5$	$\approx 17'$ to $30'$	$\sim 1'$
Baselines	36–2760 m	36–2760 m	0.3–80 m	0–614 m

Note. Haverkorn et al. (2003) fit RM $= d\chi/d(\lambda^2)$ without Faraday synthesis and thus have no ability to separate multiple Faraday depth components.

values agree in sign with that of ST+EMLS. The values of $|\chi|$ are smaller at 1420 MHz than at 614 MHz, which is consistent with the expected reduction in Faraday rotation at higher frequencies. We note some smaller structures on sub-tadpole scales in ST+EMLS data not present in CHIME, which may arise from probing larger physical depths at a higher frequency and with a much smaller beam, combining to yield a more distant polarization horizon (Uyanıker et al. 2003). In contrast, although the WSRT data have an angular resolution on the order of magnitude of the ST+EMLS data, the larger λ^2 means we expect the polarization horizon to be closer, possibly probing physical depths more similar to CHIME than to the ST+EMLS.

4.2. Faraday Depths

While the tadpole is prominent in polarization angle images, it does not stand out from the background in total intensity in single-channel images. Previous studies (Haverkorn et al. 2003; Bernardi et al. 2009; Iacobelli et al. 2013) found the head to show strong negative Faraday rotation peaking at $\phi \approx -8$ rad m^{-2}. The data sets used in these studies and their observing parameters are listed in Table 1.

We show pI images at $\phi = -15$, -7, and -3 rad m^{-2} using CHIME and WSRT 150 MHz data in Figure 6. In both data sets, the head stands out as a strong feature in pI at -7 rad m^{-2} with little surrounding emission. Furthermore, in both data sets the head appears to be a DP feature in pI at -3 rad m^{-2}, but with differing morphology; in WSRT, the entire region of the head shows little or no polarized intensity, while there is a ring of polarized intensity outside the head. This suggests *pure Faraday rotation*: the polarized intensity is moved from $\phi = -3$ to -7 rad m^{-2}. At CHIME frequencies, the -3 rad m^{-2} image shows a narrow depolarized ring immediately outside the head, but it lacks the clearly defined region of bright emission we find in WSRT. At $\phi = -15$ rad m^{-2}, a structure appears in the CHIME data, which is absent in the WSRT data. The tail of the tadpole stands out from its surroundings at this Faraday depth, with the bright emission extending partway around the head, tracing the depolarized ring that appears at the other two Faraday depths shown. The tail also appears as reduced pI at $\phi = -7$ rad m^{-2} in CHIME data.

We show Faraday spectra at three positions—one in the head, one in the tail, and a background position—in Figure 7 for CHIME and 150 MHz WSRT data. In the head, we find multiple peaks in both data sets. In the 150 MHz data, there are peaks at ≈ -8, -4, and 0 rad m^{-2}, with polarized intensities of ~ 5, 4, and 6 Jy $beam^{-1}$, respectively. In CHIME data, there is also a Faraday depth peak at $\phi \approx -8$ rad m^{-2} with $pI \approx 1.3$ Jy $beam^{-1}$, while a secondary peak is at $+5$ rad m^{-2} with $pI \approx 0.4$ Jy $beam^{-1}$. There is no evidence of a peak near -4 rad m^{-2}. However, with $\delta\phi = 9.7$ rad m^{-2} in the CHIME data, we would not expect to resolve two peaks separated by ≈ 4 rad m^{-2}. In the tail, we see two peaks in both the CHIME and 150 MHz data at $\phi \approx -2$ and -14 rad m^{-2} ($pI \approx 1.75$ and 0.35 Jy $beam^{-1}$), and $\phi \approx -4$ and -12 rad m^{-2} ($pI \approx 3.4$ and 1.8 Jy $beam^{-1}$) respectively. The CHIME peaks in both the head and tail are separated by close to $\delta\phi$, suggesting that the separation of the peaks may be an artifact of the RMSF and may not be physically meaningful, as we discuss in Section 4.3 below. Off-tadpole, we find only one peak in the CHIME data at $\phi \approx -2$ rad m^{-2} with $pI \approx 1.35$ Jy $beam^{-1}$. There is a bump in the spectrum seen at ~ 10 rad m^{-2}; however, this bump does not coincide with any notable peak in the 150 MHz data. Rather, we find two peaks at $\phi \approx -2$ and -8 rad m^{-2} with polarized intensities ≈ 4 and 3 Jy $beam^{-1}$, respectively.

Plotting the fitted peak Faraday depth values (as described in Section 3.2.2) in Galactic coordinates gives the map shown in Figure 3(b). This image lets us view the Faraday depth morphology of the region more effectively. In this image, the head of the tadpole is clearly visible, showing significant negative Faraday depths (around -7 to -8 rad m^{-2}) compared to the surrounding region (around -1 rad m^{-2}). In contrast with the single-frequency images (Stokes Q and U in Figure 2 and polarization angle in Figure 5) the tail of the tadpole does not stand out in peak Faraday depth.

4.3. Faraday Complexity

Using the peak Faraday depths in Figure 3(b), we derotated the observed polarization angle to the nominal intrinsic angle by rearranging Equation (1). The result, shown in Figure 3(c), reveals the tail as a distinct feature, separate from its background, and spatially uniform in polarization angle. If the tadpole is solely a Faraday rotation phenomenon, with a single Faraday-simple feature representing each line of sight, we would not expect it to be visible in a map of derotated χ. The fact that it *does* appear means that either the tadpole contributes significant polarized emission distinct from its surroundings, or there is Faraday complexity along the lines of sight passing through it. The latter possibility is strongly suggested by the sample Faraday depth spectra in Figure 7 and the image slices shown in Figure 6.

The separation of the two peaks in the tail in the CHIME data, ≈ 12 rad m^{-2}, is close to the separation between the main lobe and first sidelobe of the RMSF, which suggests the influence of

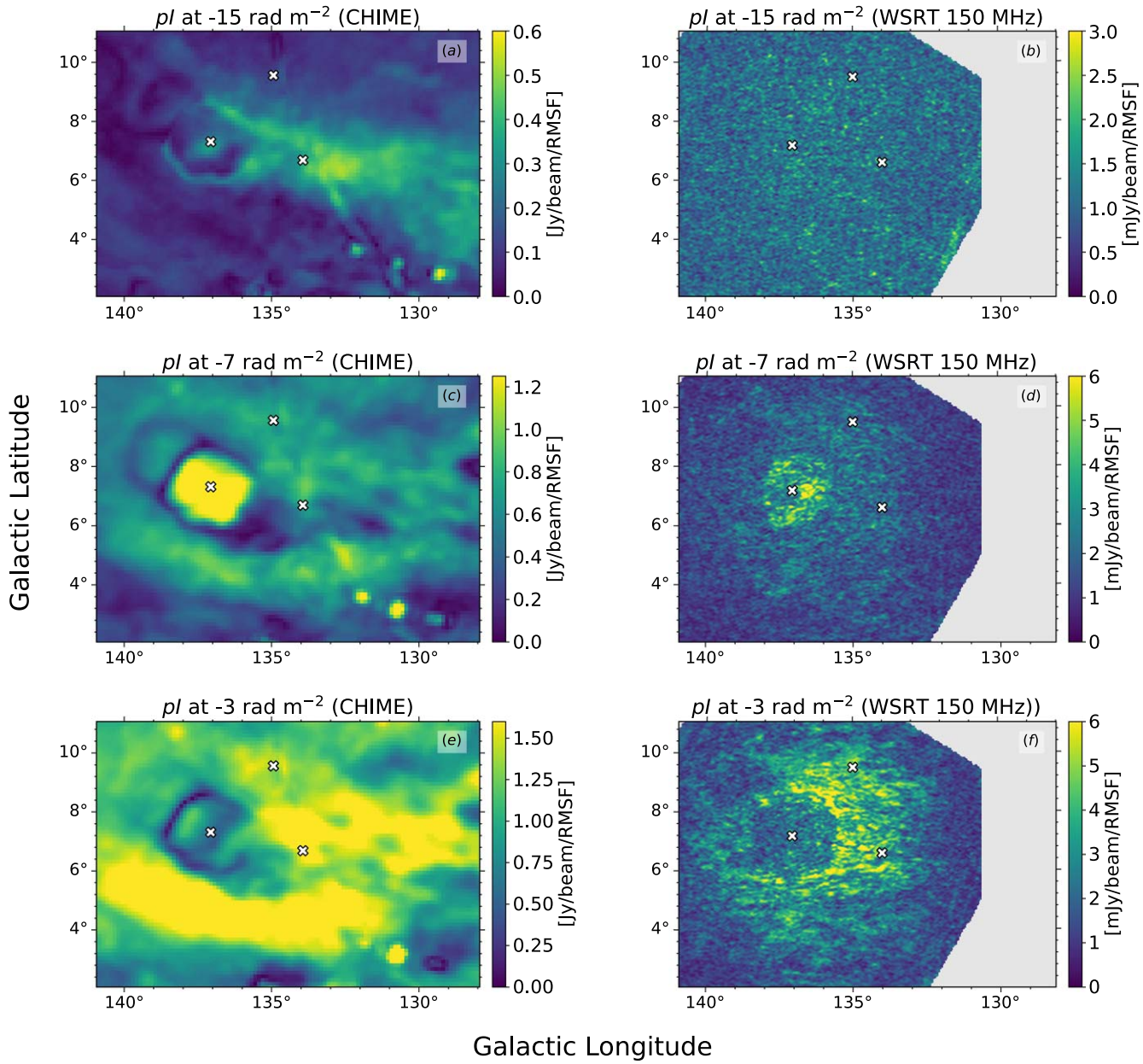

Figure 6. Images of polarized intensity at $\phi = -15$ rad m^{-2} (a), (b), -7 rad m^{-2} (c), (d), and -3 rad m^{-2} (e), (f) from CHIME 400–729 MHz data (left) and WSRT 150 MHz data (right). Note that the fainter loop above and to the left of the head, visible in all three CHIME channels but most clearly at -7 rad m^{-2}, is a grating lobe artifact; see Section 4.5.

the λ^2 coverage. In this context, the Faraday complexity is a true feature but unresolved or marginally resolved. We address this issue in Appendix A, concluding that while the *presence* of multiple peaks in the Faraday spectra is real, the *positions* of two peaks separated by $\lesssim\delta\phi$ are modified by the Faraday synthesis process, as was first demonstrated by Sun et al. (2015). *QU* fitting is less subject to this issue; in most but not all cases, *QU* fitting recovers the true Faraday depths of multiple screens even when separated by $\lesssim\delta\phi$. We investigate the validity of the secondary peaks further in the following section.

4.4. QU *Fitting*

In the CHIME Faraday depth spectra, a secondary peak at $\phi \approx -14$ rad m^{-2} appears as a coherent structure along the tail. Given the proximity of this feature to the first sidelobe of the RMSF (Figure 4), it is necessary to investigate the validity of these secondary peaks. To this end, we employed *QU* fitting, using the `qufit` package in `RM-Tools`, with the `PyMultiNest` nested sampler. We examined 51 representative lines of sight throughout the head and tail of the tadpole and in the surrounding region. We tested four models: screens at one and two Faraday depths (1 FD and 2 FD), with and without beam DP. The fractional polarization for this set of models is given by

$$\tilde{p}(\lambda^2) = \frac{\tilde{P}(\lambda^2)}{I} = \sum_k p_{0,k}\, e^{2i(\chi_{0,k}+\phi_k\lambda^2)} e^{-2\sigma_k^2\lambda^4}, \tag{8}$$

where σ_k is the standard deviation of Faraday depths within the beam, the subscript 0 refers to quantities at the source of emission, and the subscript k refers to the individual Faraday depth components (primary and secondary in our models). The

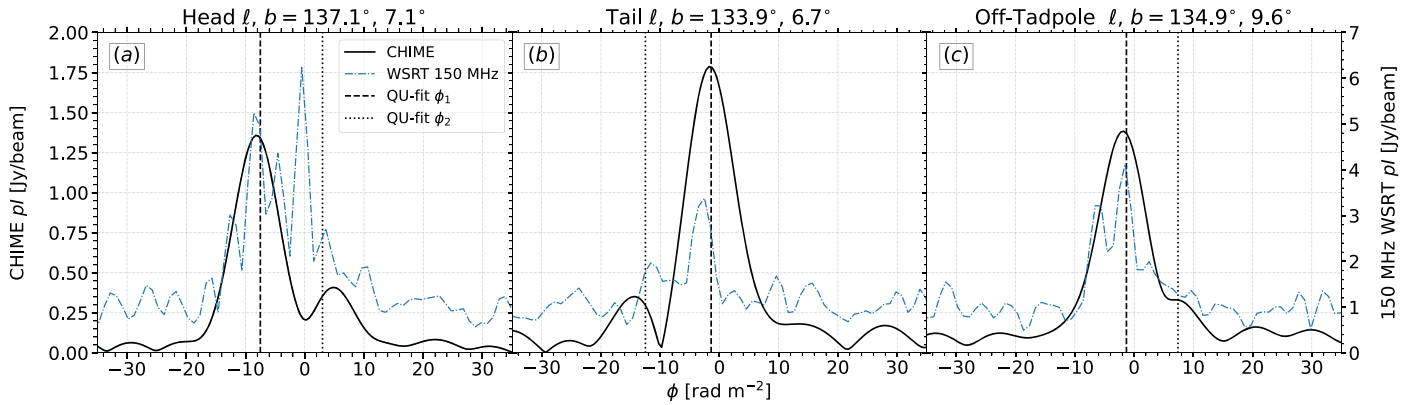

Figure 7. Faraday spectra (magnitudes) from CHIME 400–729 MHz (black solid lines) and WSRT 150MHz (blue dotted–dashed lines) for lines of sight on the tadpole head, tail, and in the surrounding region. These lines of sight correspond to the markers shown in Figure 2 and elsewhere. Dashed and dotted vertical lines show the peaks ϕ_1 and ϕ_2 from *QU* fitting (see Section 4.4). The intensity scale on the left applies to CHIME data; the intensity scale on the right applies to WSRT data.

Table 2
Results of *QU* Fitting for Representative Lines of Sight

Location	ℓ, b	p_1	ϕ_1 (rad m^{-2})	$\chi_{0,1}$	σ_1 (rad m^{-2})	p_2	ϕ_2 (rad m^{-2})	$\chi_{0,2}$	σ_2 (rad m^{-2})
Head	137.1°, 7.1°	0.46	**−7.5**	1°	1.4	0.08	**3.0**	65°	0.02
Tail	133.9°, 6.7°	0.47	**−1.4**	163°	1.3	0.15	**−12.5**	112°	2.0
Off	134.9°, 9.6°	0.26	**−1.3**	176°	0.03	0.11	**7.4**	106°	1.3

Note. Parameters refer to variables in Equation (8). Faraday depth values are bolded for ease of comparison with Faraday synthesis results.

$e^{-2\sigma_k^2\lambda^4}$ factor represents beam DP caused by any unresolved variation of ϕ within the beam. Beam DP can be caused by unresolved turbulent cells or a gradient of ϕ across the beam. Setting σ_k to zero produces the corresponding Faraday screen(s) with no beam DP, while setting $p_{0,k}$ to zero for $k > 1$ produces the one-component model.

For the nested sampling, we used uniform distributions of priors for all parameters, with $\phi_k \in [-50,\ 50]$ rad m^{-2}, $p_{0,k} \in [0,\ 1]$, $\chi_{0,k} \in [0°,\ 180°]$, and $\sigma_k \in [0,\ 100]$ rad m^{-2}. We also constrained the Faraday depths and fractional polarizations such that $|\phi_1 - \phi_2| \leqslant 100$ rad m^{-2} and $\sum_k p_{0,k} \leqslant 1$. Following Thomson et al. (2021), we use the Bayesian evidence to determine the best-fit models, as described in Appendix B.

For the three representative lines of sight shown in Figure 7, we found a two-component model with independent beam DP factors for each component to be the best fit (the full form of Equation (8)), although the primary and secondary components of the off-tadpole and head points respectively have low DP. By contrast, both components for the line of sight through the tail exhibit significant DP. The results of this model and best-fit parameters are summarized in Table 2 and Figure 8 (orange lines) for these three sample lines of sight, and the ϕ values are marked by vertical lines in Figure 7. Figure 8 also shows the three other models we tested for those lines of sight. A comparison of the models is presented in detail in Appendix B. Note that the ripples seen in the data in Figure 8 that are not fitted by the models are the well-known 30 MHz CHIME ripple caused by reflections between the cylinders and the focal line (CHIME Collaboration 2022, 2023). The Faraday depths for all 51 lines of sight tested are shown in Figure 9, with the background images indicating the first (top panel) and second (bottom panel) peaks from the Faraday depth cube, and the colors of the 51 points indicating the corresponding *QU*-fitted Faraday depths from the two-component model with DP.

In the head of the tadpole, most of the 18 tested lines of sight have a primary component near −7 rad m^{-2} (Figure 9, top panel), with some lines of sight having a weak secondary component (mostly less than $p = 0.1$; Figure 9, bottom panel). Since this secondary component is relatively weak, the head is mostly well-fit with a one-component model with DP. In the tail of the tadpole, a two-component model (with DP) is consistently the best-fit model across the 18 lines of sight tested, in contrast to the surroundings for which several of the 15 tested lines of sight are adequately described by a one- or two-component screen (without DP). Although the tail does not stand out from its surroundings in terms of the primary component (which is mostly between −2 and 0 rad m^{-2} in both the tail and the off-tadpole region), it *does* have a relatively coherent secondary component between −14 and −11 rad m^{-2}, which the surroundings lack. This is the secondary component that also appears in the Faraday depth spectra, although in some cases, it is shifted slightly in Faraday depth due to the interaction of the components with the RMSF (see Sun et al. 2015, and Appendix A).

We note that the purpose of the models we chose to test was to confirm the Faraday depth values of the primary and secondary peaks in the spectra derived using Faraday synthesis. As we can see from large values of the Bayes odds ratios listed for the models in Appendix B, the *true* description of the tadpole lines of sight is likely more complicated than this set of models.

4.5. Artifacts

The CHIME maps are sensitive to structures on a wide range of angular scales. Some artifacts are described in detail in

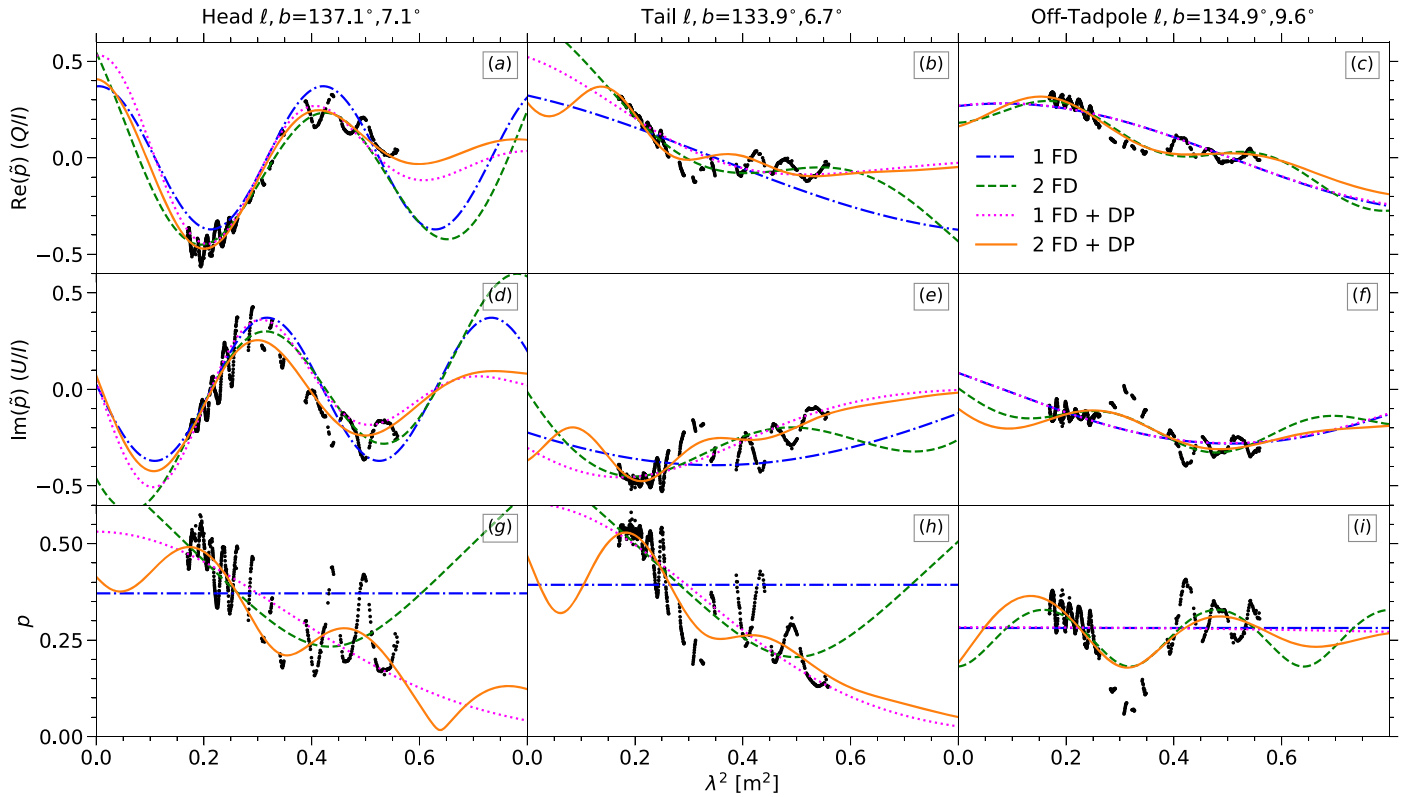

Figure 8. Best-fit models from QU fitting for the lines of sight shown in Figure 7. The panels show Q/I (a)–(c), U/I (d)–(f) and the fractional polarized intensity, p (g)–(i). Black points represent the data. The blue dotted–dashed line is the one-component model (1 FD), the green dashed line is the two-component model (2 FD), the magenta dotted line is the one-component model with beam DP (1 FD+DP), and the orange solid line is the two-component model with beam DP (2 FD+DP). The fast ripples in the data (an instrumental effect) are not fitted by the models.

CHIME Collaboration (2022). One is evident in the single diagonal stripe in the top left corner of Figures 2 and 3, which is a line at the right ascension of Tau A. Curved striations, seen in the Stokes Q and U images (Figure 2) and the Faraday synthesis images (Figure 3), correspond to fixed zenith angles (or, equivalently, declinations). Point sources appear as a single point with bright copies at the same declination on either side of the source due to grating lobes, resulting in an apparent triple source. The sources themselves appear in Stokes Q in equatorial coordinates due to leakage, with symmetric sidelobes, while in Stokes U only the asymmetric sidelobes, with opposite signs, appear. In the Galactic coordinates shown in this paper, leakage sources appear in both Q and U, along with their sidelobes.

Grating lobes also appear for larger-scale structures, having a slight effect on the appearance of the images of the tadpole region. In the CHIME 410 MHz pI map in Figure 5, a copy of the head of the tadpole can be seen as an outline that stands out in polarized intensity, centered on $\ell \approx 138\overset{\circ}{.}5$, $b \approx 8\overset{\circ}{.}5$. The location and the separation between this and the center of the head agree with the position of the grating lobes in relation to the main lobes of the point sources. This *ghost* copy of the tadpole also appears in the 410 MHz polarization angle image in Figure 5, is generally more apparent at the lower frequencies, and is quite evident in the Faraday depth slices shown in Figure 6.

There is also declination-dependent striping, which appears as curved stripes in Galactic coordinates in Figure 2 and other images, although it is much less pronounced in angle images and Faraday synthesis products. This arises from crosstalk between adjacent feeds (CHIME Collaboration 2022, Figure 18). We could remove the striping using image processing techniques, but this cosmetic improvement to the images is unnecessary for our science. Ultimately, the inclusion of the DRAO 15 m survey (A. Ordog et al. 2024, in preparation) will allow us to exclude baselines $\lesssim$5 m from the final CHIME-GMIMS data product; we expect this to considerably reduce this striping.

5. The Origin of the Tadpole

5.1. Neutral Hydrogen Structure

We turn our investigation to an analysis of the general structure of neutral hydrogen in the Galaxy's ISM in the Fan region. We use DRAO ST+HI4PI H I observations described in Section 3.3 and shown in Figure 10 for this purpose. We searched the ST+HI4PI data cube at velocities corresponding to the Local, Perseus, and Outer spiral arms (Reid et al. 2014) for emission features with a morphological resemblance to the tadpole but were unable to find any. The tadpole most likely lies within the Local Arm, corresponding to $|V_{\rm LSR}| \lesssim 30$ km s^{-1} for H I emission. Under this assumption, its physical scale is reasonable; at outer-arm distances, the head would be 170 pc in diameter. As discussed by Haverkorn et al. (2003), this is implausibly large for a single-star ionized region or any other Faraday-rotating feature. Moreover, if the tadpole is local, there will be polarized emission arising at larger distances, which can be Faraday rotated.

In an attempt to identify the structure of G137+7 in neutral hydrogen observations in regions of excess, or lack of, hydrogen, Verschuur (1969) made "*relative intensity*" profiles

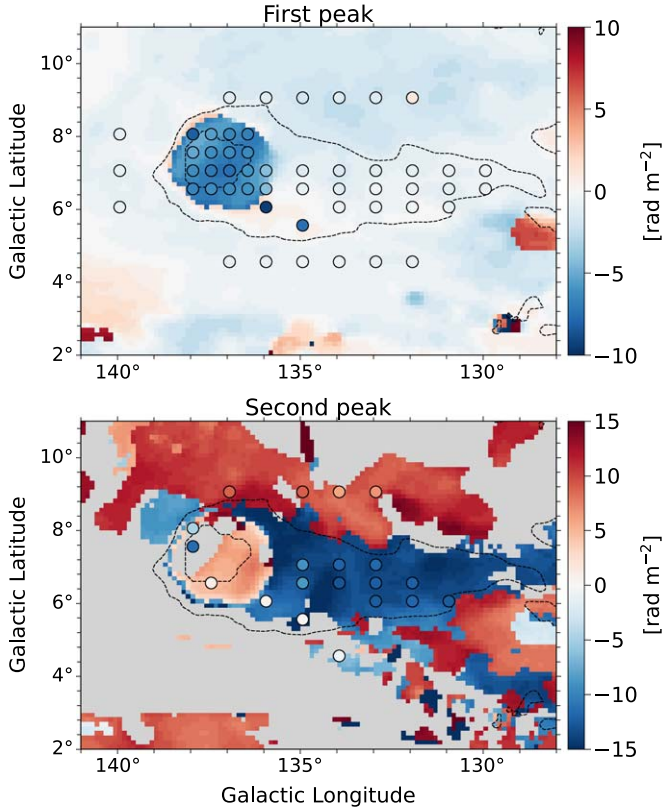

Figure 9. Results of *QU* fitting along representative lines of sight in the tadpole region, compared to Faraday synthesis results. The background images show the Faraday depth of the brightest peak in the Faraday spectrum (top panel) and the second-brightest peak (bottom panel) at each pixel. The circles show the Faraday depths derived from *QU* fitting (ϕ_1 in the top panel, ϕ_2 in the bottom panel) in 51 directions in and around the tadpole. A mask is applied in the bottom panel to exclude peaks in the spectra below the CLEAN threshold (0.2 Jy beam^{-1}; grayed out regions) and *QU*-fitted components below $p = 0.1$ (missing points).

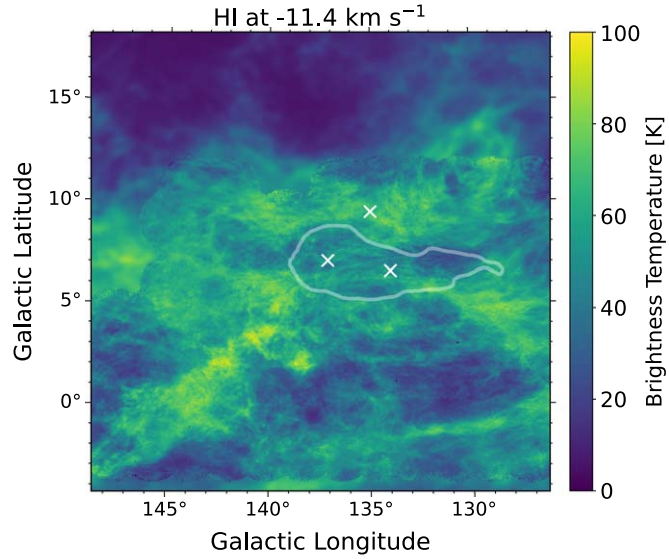

Figure 10. H I image from ST+HI4PI at Local Arm velocity of -11.4 km s^{-1}. Superimposed is a contour from the CHIME polarization angle representing the tadpole region. The "×" markers are as in Figure 2. In parts of the image where ST data are not available (mostly at $b > +12°$), we use HI4PI data instead.

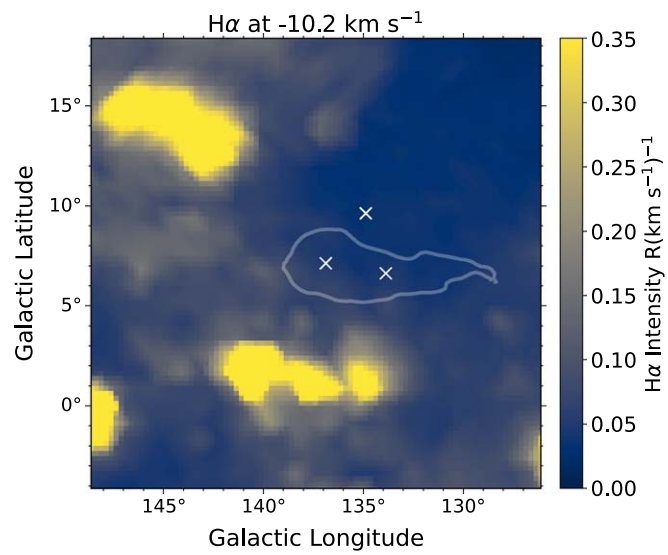

Figure 11. Hα image from the WHAM survey at the Local Arm velocity of -10.2 km s^{-1}. The contour is as in Figure 10; the "×" markers are as in Figure 2.

of H I at each velocity interval (using data from Heiles 1967). These relative intensity profiles came from drawing a baseline through the mean levels at the two highest and two lowest declinations from the scans. Then, the baselines were subtracted from the H I data to create profiles to show abundances or deficiencies in H I. From this, Verschuur (1969) identified H I deficiencies at velocities between -16 and -4 km s^{-1} that coincide with the structure G137+7 in polarization maps.

We attempted to replicate the findings of Verschuur (1969), now using the ST+HI4PI data. The ST+HI4PI data has an angular resolution of 1′, an improvement on the 12′ resolution of Heiles (1967), and both surveys have a spectral resolution of roughly 1 km s^{-1}. Searching the entire cube after subtraction, we note a weak deficit of H I at -11.4 km s^{-1} roughly coincident with the tail, showing a drop in H I of ∼50 percent relative to the immediate surroundings. However, this deficit does not match the morphology of the tail, and dips in H I intensity at this scale are very common in the HI4PI data for this area, as seen in Figure 10. We do not regard this as a significant feature.

5.2. Ionized Hydrogen Structure

Hα profiles offer a means to probe the distribution of ionized gas (Haffner et al. 2003). The WHAM survey provides us with a kinematically resolved map of the Hα emission in the Galaxy, within approximately 100 km s^{-1} of our LSR. Areas rich in ionized gas signify an enhanced population of free electrons, which play a crucial role in the Faraday rotation mechanism.

Local Arm Hα data from the WHAM survey is shown in Figure 11, where the tadpole feature does not coincide with any region of bright Hα emission. We searched the rest of the channels in the data cube and found no correspondences. The regions bright in Hα emission that are seen in Figure 11 are from documented features, namely, the three H II regions W3, W4, and W5 near $134° \lesssim \ell \lesssim 142°$ and $b \approx +1°$.

We consider the possibility that the tail is primarily due to residual ionization from a past ionization source, such as a passing hot star. If the WIM is 8000 K, the recombination

coefficient to energy levels $n \geqslant 2$ is $\alpha^{(2)} \approx 3.04 \times 10^{-13}\,\mathrm{cm}^3\,\mathrm{s}^{-1}$ (Haffner et al. 2003; Draine 2011). The recombination time is $t_r \approx (\alpha^{(2)} n_e)^{-1}$. If we assume an electron density $n_e = 0.1\,\mathrm{cm}^{-3}$ (Hill et al. 2008), this gives a recombination time of $\sim$1 Myr. Under the assumption that the ionizing source has traveled along the path laid out tail-to-head, then $\sim$1 Myr ago, the star was in the middle of the current location of the tail ($\ell \approx 132°$). The angular separation of the center of the head and halfway along the tail is about 5°, meaning the ionizing source would have a proper motion of $\sim$20 mas yr^{-1} in this model. The thinning of the tail with increasing distance from the head is consistent with this recombination scenario.

5.3. Proper Motions of Candidate Stars

Previous studies of feature G137+7 considered the circular region to be a result of a Strömgren sphere of the B2(e) star HD 20336, or alternatively, a relic Strömgren sphere from the white dwarf WD 0314+64, both of which lay within the head of the tadpole (Verschuur 1968; Iacobelli et al. 2013).

We hypothesize that the tail of the tadpole is a trail of ionized gas behind a suitable star, and should indicate motion related to the feature, potentially in the fashion suggested by Haverkorn et al. (2003) with an elongated Strömgren sphere. The tail may be similar to tails associated with planetary nebulae (Ransom et al. 2010, 2015), yielding estimates of the timescales for the interactions of planetary nebulae and the ISM. For a star to be considered a strong candidate for the tadpole, the characteristics we observe require it to be a hot star (Type O or B) with a proper motion comparable to our calculations based on the recombination time (see Section 5.2) and direction aligned with the orientation of the tail.

We check to see whether the motion of HD 20336 meets these criteria. We overlay the inferred positions over the past 3 Myr of HD 20336 given the sky-projected space velocity calculated from Gaia proper motion values (Gaia Collaboration et al. 2023), corrected for the LSR (e.g., Soderblom et al. 1989; Ransom et al. 2015) given by Huang (2015) atop Figure 2. The orientation of the tadpole is just outside the error cone of the trajectory we determined for HD 20336, suggesting that an association is possible but not definitive. The error in the path of HD 20336 is largely from the uncertainty in the LSR. The orientation of the tail parallel to the Galactic plane also suggests motion in the plane, as might be expected for a star. Similar corrected space velocity values were calculated for WD 0314+64, finding a proper motion path that agreed less well with the tail. The angular velocities of the B2(e) star and white dwarf are 9.98 ± 0.02 and 159.4 ± 0.1 mas yr^{-1}, respectively. The high angular velocity of the white dwarf rules it out based on the timescale estimates we find for the tail in Section 5.2 (unless $n_e \sim 1\,\mathrm{cm}^{-3}$, which is much higher than typical in the WIM); however, the B2(e) star's angular velocity is of the same order of magnitude as our estimates—a result consistent with the star causing the feature. Using the Gaia database, we searched[26] for any other candidate stars that could cause the Faraday rotation feature (Anderson et al. 2024). We identified no new candidates from this query.

5.4. Faraday Depth and Electron Column

We can make sense of the absence of the tadpole in both the ST+HI4PI H I and WHAM surveys by considering that the strongest observed Faraday rotation in the head is $\phi \approx -8\,\mathrm{rad\,m}^{-2}$. This requires free electrons that would have been ionized from neutral hydrogen in the ISM. Here, we assume that a change in the electron density, not a change in the magnetic field, is the dominant factor in the change in ϕ. This would leave a deficit in the neutral hydrogen column density, N(H I), but as demonstrated above, we do not observe this. The magnitude of change in the H I density needed to produce the observed Faraday depth can be estimated using (from Equation (2)) $\phi = 0.81 \cdot n_e B_{\|} L$. Using the Faraday depth from the head of the tadpole and the canonical total magnetic field strength in the Solar neighborhood of 6 μG (Haverkorn 2015), the change needed in the column density of free electrons is $n_e L \sim 1.5 \times 10^{18} B_6^{-1}\,\mathrm{cm}^{-2} \sim 1.4 B_6^{-1}\,\mathrm{pc\,cm}^{-3}$, or an emission measure of $\mathrm{EM} \equiv \int n_e^2\, ds = (n_e L)^2/L \sim 2(L/1\,\mathrm{pc})^{-1} B_6^{-2}\,\mathrm{pc\,cm}^{-6}$. Here, we define $B_6 \equiv B_{||}/6\,\mu\mathrm{G}$; $B_6 = 1/\sqrt{3}$ if a 6 μG field is randomly distributed among three orthogonal components.

If the free electrons arose from the ionization of existing neutral hydrogen, this would result in a decrease in N(H I) of $\sim 1.5 \times 10^{18} B_6^{-1}\,\mathrm{cm}^{-2}$. This is small compared to the typical $N(\mathrm{H\,I}) \gtrsim 10^{20}\,\mathrm{cm}^{-2}$ near the plane (less than 3% in the case of $B_6 = 1/\sqrt{3}$) and thus would be impossible to see as a deficit in H I maps. An emission measure of $\approx$2 pc cm^{-6} would be detectable in Hα emission (Haffner et al. 2003); if the path length of ionized gas were $L \gtrsim 3$ pc, the emission measure would be less than the 3σ sensitivity of the WHAM survey ($\mathrm{EM} \sim 0.3\,\mathrm{pc\,cm}^{-6}$). Therefore, Faraday rotation would be sensitive to a change in electron column density that could not be detected in other tracers even if there were no change in the magnetic field. Because we would not expect to detect a change in $n_e L$ in other tracers, we cannot readily distinguish between a change in the electron column and a change in $B_{||}$. The motion of ionized gas may distort the magnetic field lines, changing their orientation with respect to the line of sight, which can also lead to a gradient in Faraday depth, a so-called *magnetic wake* (Ransom et al. 2010).

6. Summary and Future Prospects

In this paper, we have presented the first polarization maps from CHIME in what will be a component of the GMIMS low-band north all-sky survey. The wide bandwidth at relatively low frequencies (400–729 MHz) gives us a Faraday depth resolution, which is roughly half the largest scale we are sensitive to, enabling investigation of Faraday complexity. We analyzed a relatively small region of the sky where the emission is bright and instrumental properties are best understood; in future work, we will expand the use of CHIME data to analyze the large-scale structure of the Galactic magnetic field.

The polarized structure that we refer to as the tadpole is composed of a circular head centered on $\ell = 137°$, $b = +7°$ roughly 2° in diameter, with a tail extending about 10° to $\ell = 127°$. The entire feature has an observed polarization angle rotated significantly compared to the surrounding sky due to Faraday rotation. The largest Faraday depth $|\phi|$ is in the head of the tadpole, with values as large as $-8\,\mathrm{rad\,m}^{-2}$. The tail appears as a second Faraday depth component at $\approx -12\,\mathrm{rad\,m}^{-2}$. The tail has been hinted at previously but is very clear both in single-channel polarization angle images and in Faraday depth images with CHIME. Similarly, what we identify as the head has been seen primarily as a DP feature in the past. With the angular and

[26] We used the capabilities of a natural language model to construct ADQL search queries of the Gaia archive (OpenAI 2023).

Faraday depth resolution of CHIME, we clearly identify it as a Faraday rotation feature, recovering most of the power that is depolarized with poorer angular or Faraday depth resolution.

The presence of a tail suggests motion along its direction through the ISM. The proper motion of HD 20336 is marginally consistent with the orientation of the tail. The tadpole is not seen in maps of neutral or ionized hydrogen column density, although our estimates suggest that the amount of gas necessary to undergo ionization, resulting in the observed Faraday rotation magnitude, falls below the sensitivity threshold of Hα and H I surveys, especially given the intensity of surrounding emission. We find the recombination time for the ionized electrons to be $\sim$1 Myr, and with this estimate, we derive a proper motion of the (unknown) ionizing source of $\sim$20 mas yr^{-1}, which is on the order of magnitude of the B2(e) star's velocity. Although this is suggestive evidence, we cannot be certain that the B2(e) star is linked to the tadpole.

The CHIME Stokes Q and U cubes covering the 400 $-$729 MHz range comprise the primary data set used in this study. This frequency coverage yields a Faraday depth resolution of 9.7 rad m^{-2}, resolving the maximum ϕ scale of $\sim$19 rad m^{-2}. Given the asymmetries present in the main lobes of some of the spectra we observe on or near the tadpole feature, exploring this region with improved ϕ resolution combined with sensitivity to extended features will be valuable.

In the longer term, we will be able to combine ϕ resolution and improved spatial resolution with the advent of the upgraded DRAO ST, which will cover 400–1800 MHz at 1′ resolution (compared to the single-frequency channel available from the current ST). The single-channel 1′-resolution χ map from the DRAO ST+EMLS in Figure 5 already reveals an abundance of structures on scales much smaller than the size of the tadpole, and investigating these in ϕ space with high resolution may provide further insights into the nature of the overall structure. Other future studies may also include exploring potential correlations between the tadpole Faraday structure and thermal dust emission features in three-dimensional dust maps.

There are three factors in this study that CHIME makes possible. First, for the purpose of this study, CHIME is effectively a large single antenna, with sensitivity to large structures, coupled with better angular resolution than the single antennas that have been used for polarimetry in this frequency range. Second, the wide bandwidth and many frequency channels enable Faraday synthesis with $\phi_{\max-\mathrm{scale}} \approx 2\delta\phi$, comfortably resolving the maximum scale. Third, the polarized sky is Nyquist sampled. This powerful combination has revealed an extended and Faraday complex structure in G137+7, a region that has been a curiosity for six decades.

Acknowledgments

This paper relies on observations obtained using telescopes located at the Dominion Radio Astrophysical Observatory, which is located on the traditional, ancestral, and unceded territory of the syilx people. We benefit enormously from the stewardship of the land by the syilx Okanagan Nation and the radio frequency interference environment protection work by the syilx Okanagan Nation and DRAO. We acknowledge the DRAO staff, especially K. Phillips and B. Robert, for their work on the site and the telescopes used in this work. DRAO is a national facility operated by the National Research Council Canada. CHIME is funded by grants from the Canada Foundation for Innovation (CFI) 2012 Leading Edge Fund (Project 31170), the CFI 2015 Innovation Fund (Project 33213), and by contributions from the provinces of British Columbia, Québec, and Ontario. Additional support was provided by the University of British Columbia, McGill University, and the University of Toronto. CHIME also benefits from several NSERC Discovery Grants, including RGPIN-2020-05035 and 569654. This research was enabled in part by support provided by the Digital Research Alliance of Canada.

A.S.H. and A.O. acknowledge Interstellar Institute's program "II6" and the Paris-Saclay University Institut Pascal for hosting discussions that nourished the development of the ideas behind this work, especially with R. A. Benjamin. We thank R. Mckinven for useful discussions about instrumental polarization in CHIME/FRB data. We also acknowledge helpful discussions with W. Raja. We thank the anonymous referee for a careful and constructive report, which led to an improved paper.

N.M. was supported by an Undergraduate Research Award from the UBC Okanagan Irving K. Barber Faculty of Science and an NSERC Undergraduate Student Research Award. A.O. is partly supported by the Dunlap Institute at the University of Toronto. A.B. acknowledges financial support from the INAF initiative "IAF Astronomy Fellowships in Italy," grant name MEGASKAT. M. Haverkorn acknowledges funding from the European Research Council (ERC) under the European Union's Horizon 2020 research and innovation program (grant agreement No. 772663). We acknowledge the support of NSERC, funding reference number 569654. K.W.M. holds the Adam J. Burgasser Chair in Astrophysics and is supported by NSF grants (2008031, 2018490). M.T. is supported by the Banting Fellowship (Natural Sciences and Engineering Research Council Canada) hosted at Stanford University.

Data Availability

FITS files containing the CHIME data products, Stokes I, Q, U, and V as a function of frequency and Faraday depth for the regions shown in this paper, are available through the Canadian Astronomical Data Centre (CHIME & GMIMS collaborations 2024): doi:10.11570/24.0001.

Facilities: CHIME, DRAO:Synthesis Telescope, Effelsberg.

Software: Astropy (Astropy Collaboration et al. 2022); `ch_pipeline`; `Matplotlib` (Hunter 2007); `NumPy`; `RM-Tools` (Purcell et al. 2020).

Appendix A
Resolved and Unresolved Faraday Components in Faraday Synthesis

In this appendix, we model the impact of resolved and unresolved Faraday depth components on Faraday synthesis spectra, similar to the analysis of Sun et al. (2015), but covering the much broader λ^2 range corresponding to the CHIME frequency coverage. We create a model with Faraday depth components ϕ_k with polarization fractions $p_{0,k}$ emitted at polarization angles $\chi_{0,k}$. The observed complex polarization is then given by Equation (8). We performed a series of simulations with the inputs listed in Table A1. We set $\sigma_k = 0$ rad m^{-2} in all cases; making σ_k nonzero produces results that are similar to reducing $p_{0,k}$ for each component. We

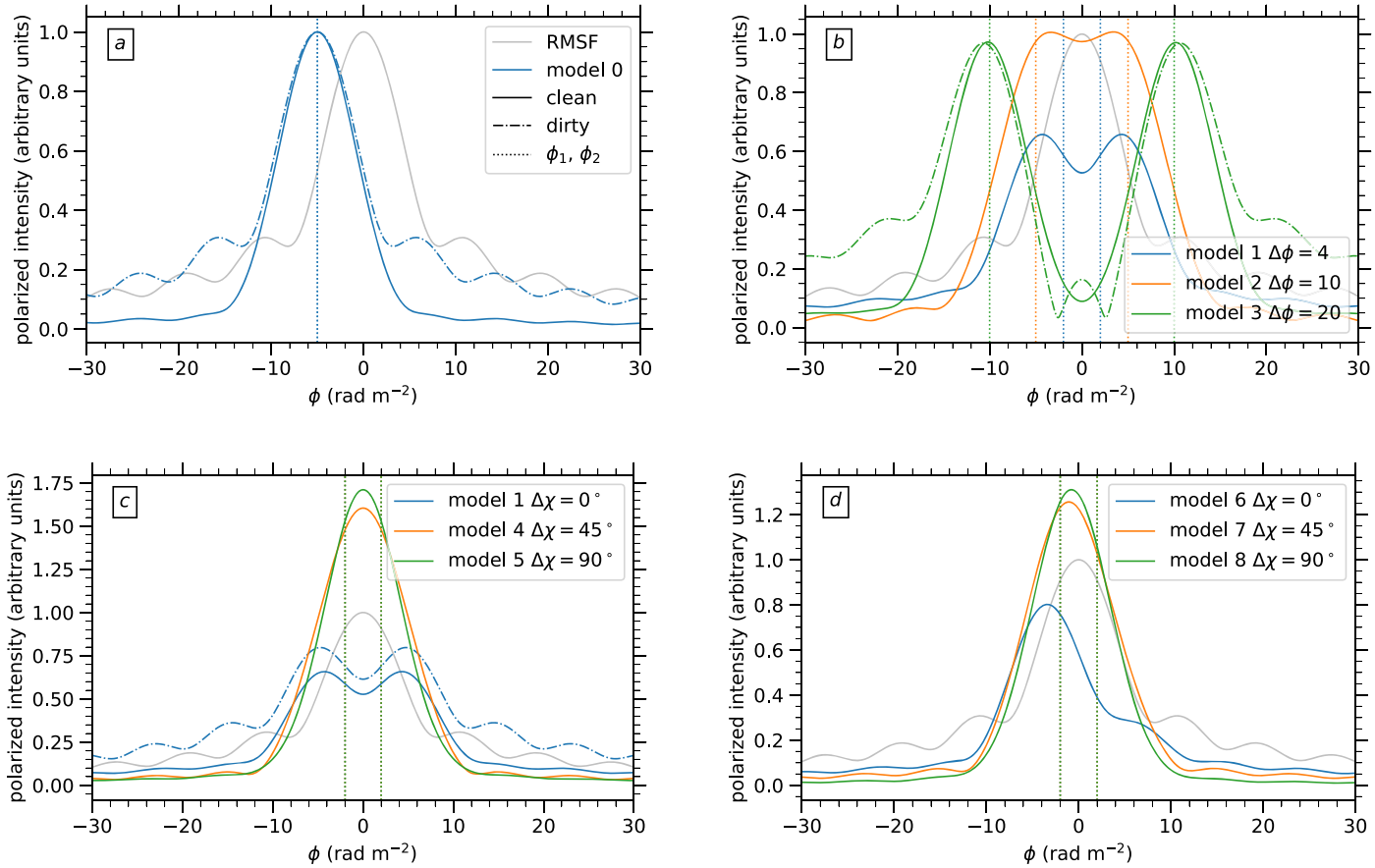

Figure A1. Output of models from Table A1. Vertical dotted lines show the input Faraday depths ϕ_1 and ϕ_2. We show dirty (dotted–dashed lines) and clean (solid lines) spectra for a few cases but clean spectra only in most cases to reduce clutter. (a) Our control model with one component at -5 rad m^{-2}. (b) Models 1–3 with two components separated by 4, 10, and 20 rad m^{-2}. (c) Models 1, 4, and 5, with two components separated by 4 rad m^{-2}, which is not resolved by the RMSF. We show the same model but with χ_2 ranging from 0 (model 1, as in panel (b) to 90° (model 5). (d) Models 6–8, with two components separated by 4 rad m^{-2}, which is not resolved by the RMSF. The second component has reduced pI. As in models 1, 3, and 4, we show the same model but with χ_2 ranging from 0 (model 5) to 90° (model 7).

Table A1
Model Parameters Shown in Figure A1

Model	$p_{0,1}I$	ϕ_1	$\sigma_{0,1}$	$\chi_{0,1}$	$p_{0,2}I$	ϕ_2	$\sigma_{0,2}$	$\chi_{0,2}$
0	1.0	-5 rad m^{-2}	0.0 rad m^{-2}	0°	0.0	⋯	⋯	⋯
1	1.0	-2 rad m^{-2}	0.0 rad m^{-2}	0°	1.0	2 rad m^{-2}	0.0 rad m^{-2}	0°
2	1.0	-5 rad m^{-2}	0.0 rad m^{-2}	0°	1.0	5 rad m^{-2}	0.0 rad m^{-2}	0°
3	1.0	-10 rad m^{-2}	0.0 rad m^{-2}	0°	1.0	10 rad m^{-2}	0.0 rad m^{-2}	0°
4	1.0	-2 rad m^{-2}	0.0 rad m^{-2}	0°	1.0	2 rad m^{-2}	0.0 rad m^{-2}	45°
5	1.0	-2 rad m^{-2}	0.0 rad m^{-2}	0°	1.0	2 rad m^{-2}	0.0 rad m^{-2}	90°
6	1.0	-2 rad m^{-2}	0.0 rad m^{-2}	0°	0.5	2 rad m^{-2}	0.0 rad m^{-2}	0°
7	1.0	-2 rad m^{-2}	0.0 rad m^{-2}	0°	0.5	2 rad m^{-2}	0.0 rad m^{-2}	45°
8	1.0	-2 rad m^{-2}	0.0 rad m^{-2}	0°	0.5	2 rad m^{-2}	0.0 rad m^{-2}	90°

Note. Input parameters used with Equation (8) to create Figure A1.

then performed Faraday synthesis on the resulting $\tilde{P}(\lambda^2)$ spectra and `CLEANed` the spectra to a threshold of $pI = 0.2$ in the arbitrary units used in these figures, producing the Faraday depth spectra shown in Figure A1. We used complete frequency coverage from 400–729 MHz in running these simulations, an idealized version of the portion of the CHIME data used in this paper, with the FWHM of $R(\phi)$ being $\delta\phi = 9.7$ rad m^{-2}. Accounting for the gaps in our frequency coverage produces additional sidelobes in the dirty spectrum but does not change the qualitative picture.

First, in Figure A1(a), we show a model with a single component at $\phi = -5$ rad m^{-2}. The dirty spectrum is an exact replica of the RMSF, shifted to the input Faraday depth. Cleaning removes the sidelobes effectively.

Next, in Figure A1(b), we show cases in which there are two components that are separated by 4 rad m^{-2}, which is

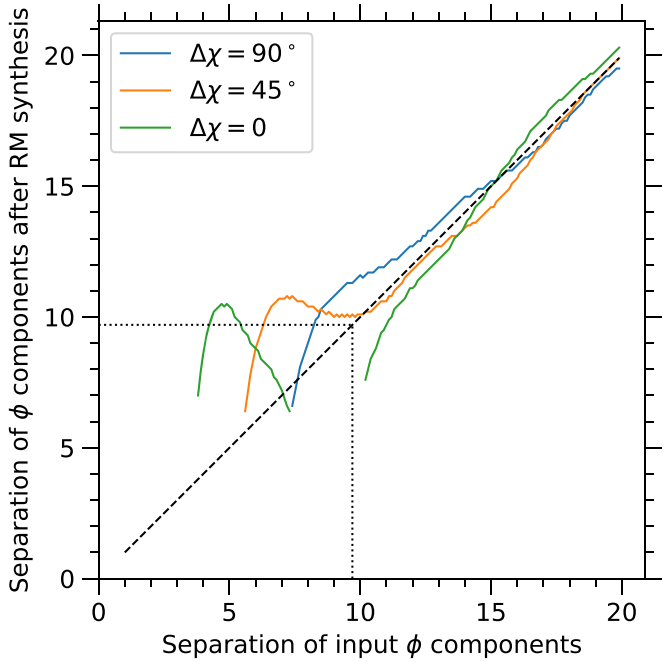

Figure A2. Output separation of Faraday depth components (calculated using Faraday synthesis) as a function of the input separation of Faraday depth components in the simulation. The dashed line shows a 1:1 line, and the dotted box shows the FWHM of $R(\phi)$ (9.7 rad m^{-2}). We ran this experiment for $1 < \phi < 20$ rad m^{-2} in 0.1 rad m^{-2} increments; outputs for which there are not separate peaks in the output Faraday spectrum are blank.

unresolved (model 1); separated by 10 rad m^{-2}, which is marginally resolved (model 2), and separated by 20 rad m^{-2}, more than twice $\delta\phi$ (model 3). In the resolved case (model 3), two peaks appear at their input Faraday depths. Sidelobes are present but removed precisely by cleaning, leaving two peaks that closely resemble Gaussians. We performed the same experiment with a wide range of input angles $\chi_{0,2}$; there is no appreciable change in the resulting Faraday spectrum. For the $\Delta\phi = 10$ rad m^{-2} case (model 2), there is a flattened appearance to the blended peaks in the Faraday spectrum. There are two peaks, but they are separated by $\approx$8 rad m^{-2}, less than the separation of the input Faraday depths. Lastly, in the unresolved case ($\Delta\phi = 4$ rad m^{-2}; model 1), there are two distinct peaks but they are separated by $\approx$9 rad m^{-2}.

In Figure A1(c), we again show two components with equal polarized intensity separated by 4 rad m^{-2}, which is not resolved by the RMSF. Model 1, with the same χ_0 in both components, is as in Figure A1(b). When the two components are emitted at different angles (45° different in model 3 and 90° different in model 4), we see only a single component centered between the two input components. These two peaks are true features in that they correspond to two distinct but unresolved input components, but their observed Faraday depths are not accurate. Instead, the Faraday depths of the observed peaks are separated by $\approx\delta\phi$. Because these peaks represent true features, they are not removed by `RM-CLEAN`, but their position is also not changed (or perhaps changed very slightly). In contrast, the sidelobes at $\pm$15 and $\pm$23 rad m^{-2} are removed by `RM-CLEAN`.

In Figure A1(d), we show a similar experiment but the intensity of one of the input components is reduced by 50%. In the in-phase model (model 5), the two peaks remain present and remain pushed out to be separated by $\approx\delta\phi$. In the out-of-phase models (6 and 7), only one peak is evident, centered at the intensity-weighted mean of the two input components.

We ran models of types 1, 4, and 5 (equal input polarized intensities with three different angular separations of the components), but now for a range of input Faraday depth separations between the components and then determined the separation of the peaks in Faraday spectra. We show the results in Figure A2 (similar to Figure 4 of Sun et al. 2015, but with a denser sampling of $\Delta\phi$). At $\Delta\phi \gtrsim 12$ rad m^{-2}, the components are resolved by Faraday synthesis and the output peaks correspond well with the input peaks. We do not observe peaks in the Faraday spectrum, which are appreciably closer than the FWHM of $R(\phi)$, 9.7 rad m^{-2}.

What causes the observed peaks in the Faraday spectrum to be at separations wider than the input values? This is a DP effect. Absent DP, we would expect two unresolved components to appear in a single, broadened Gaussian-like form. When the Faraday-rotated emission from the two components is out of phase, DP occurs. With two Faraday screens of equal pI, the Faraday spectrum $\tilde{F}(\phi)$ is the sum of two copies of the RMSF with centroids separated by $\phi_2 - \phi_1$. The imaginary part of $\tilde{R}(\phi)$ is antisymmetric, so for certain separations of ϕ_1 and ϕ_2, the imaginary parts of the copies of $\tilde{R}(\phi)$ interfere and depolarize. From these investigations, we conclude that Faraday synthesis results should be interpreted with caution when the spacing of peaks is $\lesssim\delta\phi$ (Equation (3)), in agreement with the similar results at higher frequencies presented by Sun et al. (2015). In this case, QU fitting, which is less sensitive to this type of interaction between Faraday depth components, should be used to refine the results.

Appendix B
QU-fitting Results

Here, we present a comparison between the Faraday synthesis and QU-fitting results for the CHIME data in terms of the Faraday depth spectra, along with a comparison of the four models tested. For the three lines of sight shown in Figures 6 and 7, we determine the complex polarized fraction, $\tilde{p}(\lambda^2)$, from the best-fit parameters resulting from QU fitting for the four models we tested: one- and two-component Faraday screens (1 FD and 2 FD), with and without beam DP. These are shown in Figure 8 for comparison in the λ^2 domain. In Figure 9 we show the Faraday depths derived from the two-component model that includes beam DP, 2 FD + DP.

We apply Faraday synthesis to each model $\tilde{p}(\lambda^2)$ determined from QU fitting. We show the resulting Faraday depth spectra, compared to the spectra derived from the data $\tilde{p}(\lambda^2)$ in Figures B1–B3. For all three lines of sight, the two-component, beam-depolarized model (2 FD + DP) spectrum agrees well with the spectrum derived from the data $\tilde{p}(\lambda^2)$. Note that small discrepancies between the data spectra shown in Figure 7 and the spectra shown here arise because the latter were calculated from Q/I and U/I (no spectral index) rather than Q and U (including spectral index) as were used for the main analysis. The off-tadpole line of sight shown in Figure B3(d) is an example of the type of scenario described in Appendix A and depicted in Figure A1(d) (model 8), in which two Faraday depth components (denoted by the vertical black lines in both of the two-component models) become slightly shifted with respect to each other through the Faraday synthesis process.

In Table B1, we summarize the best-fit parameters of all models for these three lines of sight, along with the Bayesian

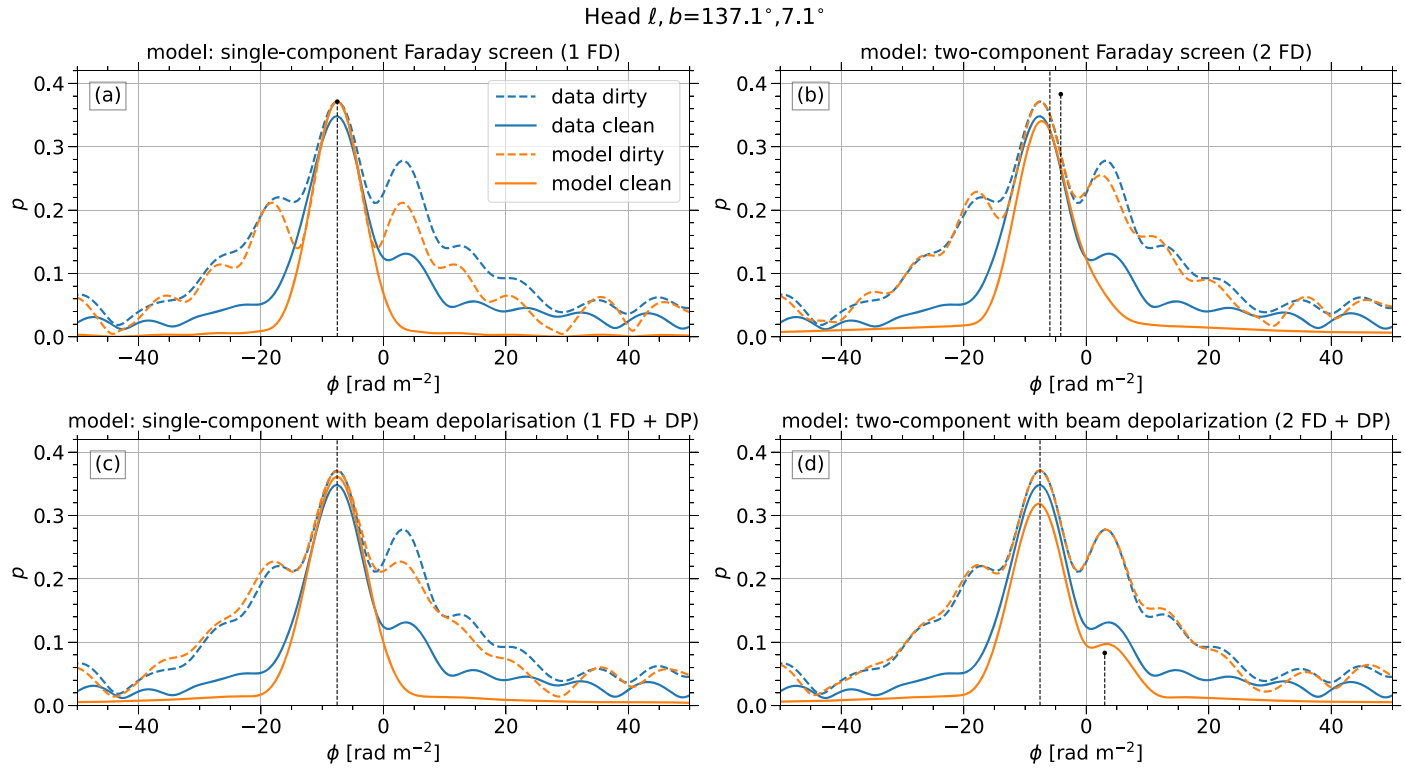

Figure B1. Results of *QU* fitting used as input to Faraday synthesis for a line of sight on the head of the tadpole for the four models described in Section 4.4. Blue lines represent the magnitudes of the spectra derived from applying Faraday synthesis to the CHIME $\tilde{p}(\lambda^2)$ data. Orange lines are the magnitudes of the spectra derived from applying Faraday synthesis to the model $\tilde{p}(\lambda^2)$ determined from *QU* fitting. Solid (dashed) lines represent clean (dirty) spectra. Vertical, black dotted lines indicate the locations of the *QU*-fitted Faraday depth components, and the black dot indicates the polarized fraction corresponding to that component.

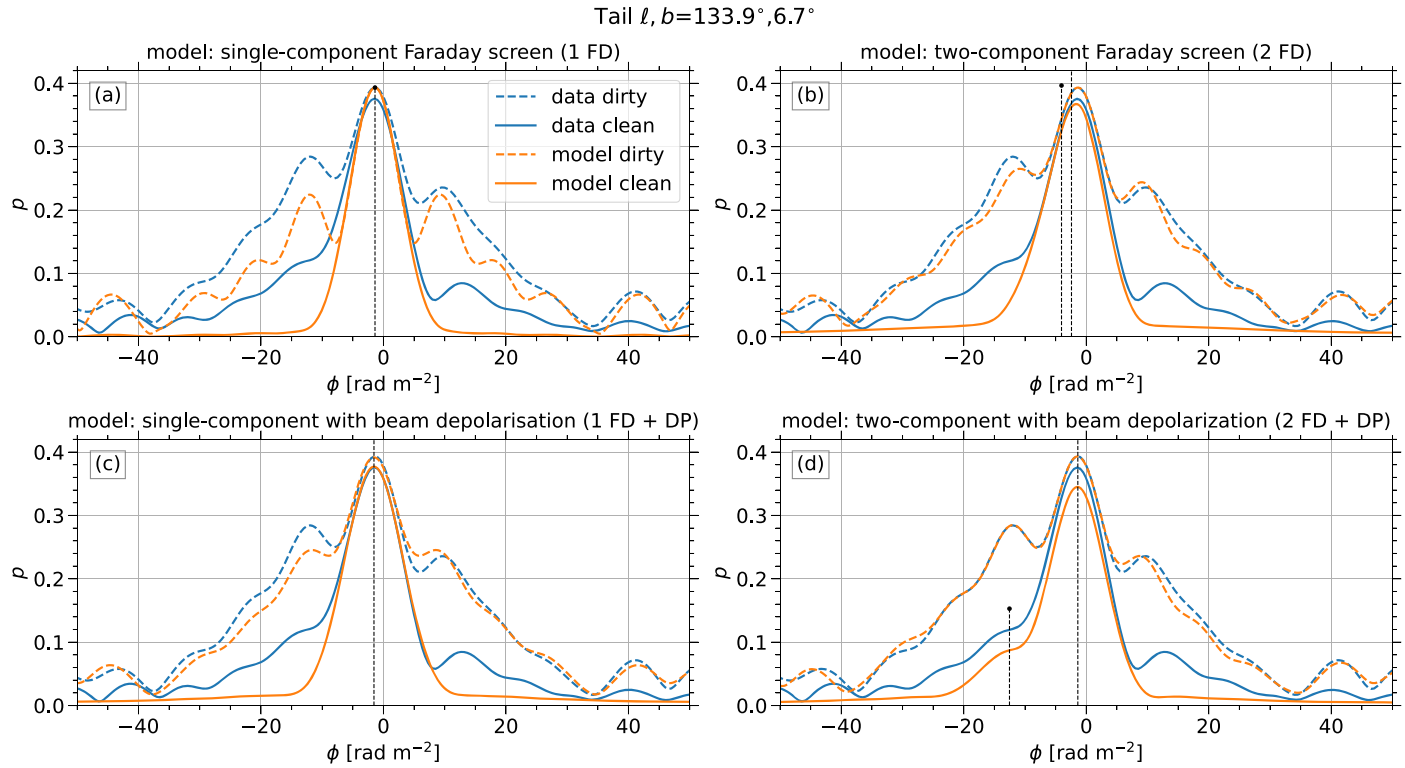

Figure B2. Results of *QU* fitting used as input to Faraday synthesis for a line of sight on the tail of the tadpole. See Figure B1 for a full description.

evidence, Z, and the Bayes odds ratio, $\Delta \ln(Z)$, to quantify the comparison between the models. We compare all models, m, to 2 FD + DP, which has the highest value of $ln(Z)$, such that

$$\Delta \ln(Z_{\rm m}) = \ln(Z_{2\ {\rm FD}\ +\ {\rm DP}}) - \ln(Z_{\rm m}). \quad \text{(B1)}$$

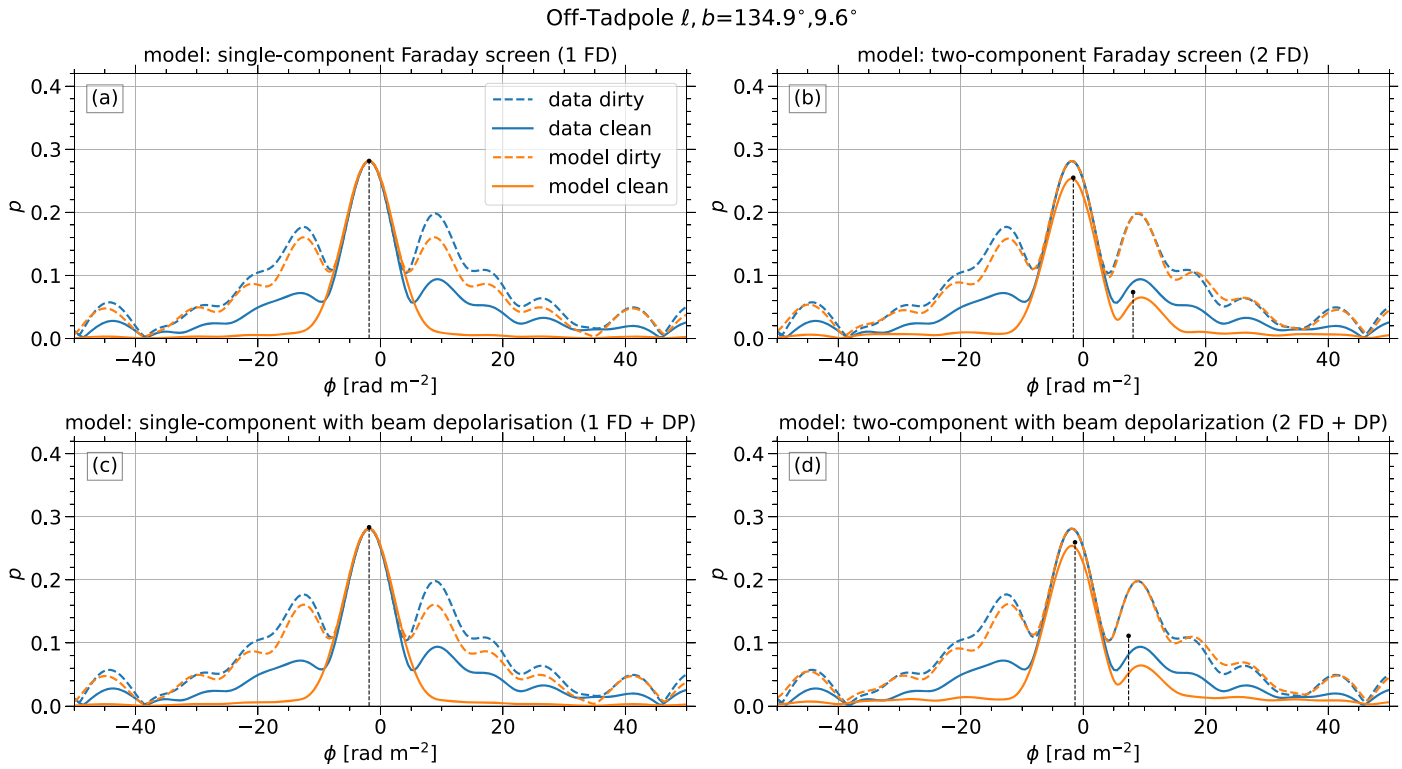

Figure B3. Results of QU fitting used as input to Faraday synthesis for a line of sight in the off-tadpole region. See Figure B1 for a full description.

Table B1
QU-fitting Results for Representative Lines of Sight

Location	ℓ, b	Model	$\ln(Z)$ ($\times 10^2$)	$\Delta\ln(Z)$ ($\times 10^3$)	p_1	ϕ_1 (rad m^{-2})	$\chi_{0,1}$	σ_1 (rad m^{-2})	p_2	ϕ_2 (rad m^{-2})	$\chi_{0,2}$	σ_2 (rad m^{-2})
Head	137°, 7°	1 FD	−53.4	37.5	0.4	−7.5	2°.0					
		2 FD	−27.0	11.1	0.6	−5.9	143°.8		0.4	−4.2	9°.6	
		1 FD + DP	−27.7	11.8	0.5	−7.6	2°.4	1.4				
		2 FD + DP	−15.9	0.0	0.5	−7.5	0°.6	1.4	0.1	3.0	65°.3	0.02
Tail	134°, 6.5°	1 FD	−57.3	49.2	0.4	−1.4	162°.7					
		2 FD	−13.4	5.3	0.6	−2.4	15°.7		0.4	−4.0	152°.2	
		1 FD + DP	−16.7	8.6	0.6	−1.6	164°.9	1.6				
		2 FD + DP	−8.1	0.0	0.5	−1.4	163°.2	1.3	0.2	−12.5	112°.5	2.0
Off	135°, 9°	1 FD	−14.9	9.8	0.3	−1.9	8°.8					
		2 FD	−5.7	0.6	0.3	−1.6	1°.5		0.1	8.1	93°.2	
		1 FD + DP	−14.9	9.8	0.3	−1.9	8°.8	0.18				
		2 FD + DP	−5.1	0.0	0.3	−1.3	175°.5	0.03	0.1	7.4	106°.3	1.3

For the selected points in the head and tail of the tadpole, a two-component beam-depolarized model (2 FD + DP) is clearly the best fit, while for the selected off-tadpole point a two-component model without DP (2 FD) may be sufficient within the set of models explored here. As noted in Section 4.4, a full description of the lines of sight toward the tadpole likely includes more complexity than this basic set of models. The primary Faraday depth components, ϕ_1, are reasonably consistent between these models, while in the head and tail of the tadpole, the secondary component, ϕ_2, is strongly dependent on whether or not beam DP is included in the model.

ORCID iDs

Nasser Mohammed https://orcid.org/0009-0008-1224-0382
Anna Ordog https://orcid.org/0000-0002-2465-8937
Rebecca A. Booth https://orcid.org/0000-0001-5181-6673
Andrea Bracco https://orcid.org/0000-0003-0932-3140
Jo-Anne C. Brown https://orcid.org/0000-0003-4781-5701
Ettore Carretti https://orcid.org/0000-0002-3973-8403
John M. Dickey https://orcid.org/0000-0002-6300-7459
Simon Foreman https://orcid.org/0000-0002-0190-2271
Mark Halpern https://orcid.org/0000-0002-1760-0868
Marijke Haverkorn https://orcid.org/0000-0002-5288-312X

Alex S. Hill https://orcid.org/0000-0001-7301-5666
Gary Hinshaw https://orcid.org/0000-0002-4241-8320
Joseph W. Kania https://orcid.org/0000-0002-3354-3859
Roland Kothes https://orcid.org/0000-0001-5953-0100
T. L. Landecker https://orcid.org/0000-0003-1455-2546
Joshua MacEachern https://orcid.org/0000-0001-8064-6116
Kiyoshi W. Masui https://orcid.org/0000-0002-4279-6946
Aimee Menard https://orcid.org/0009-0007-6503-1501
Ryan R. Ransom https://orcid.org/0000-0003-2469-1611
Wolfgang Reich https://orcid.org/0000-0002-5313-6409
Patricia Reich https://orcid.org/0009-0006-8615-8352
J. Richard Shaw https://orcid.org/0000-0002-4543-4588
Seth R. Siegel https://orcid.org/0000-0003-2631-6217
Mehrnoosh Tahani https://orcid.org/0000-0001-8749-1436
Alec J. M. Thomson https://orcid.org/0000-0001-9472-041X
Tristan Pinsonneault-Marotte https://orcid.org/0000-0002-9516-3245
Haochen Wang https://orcid.org/0000-0002-1491-3738
Jennifer L. West https://orcid.org/0000-0001-7722-8458
Maik Wolleben https://orcid.org/0009-0006-9479-7509
Dallas Wulf https://orcid.org/0000-0001-7314-9496

References

Anderson, R. I., Koblischke, N. W., & Eyer, L. 2024, ApJ, 963, L43
Astropy Collaboration, Price-Whelan, A. M., Lim, P. L., et al. 2022, ApJ, 935, 167
Bell, M. R., & Enßlin, T. A. 2012, A&A, 540, A80
Berkhuijsen, E. M., Brouw, W. N., Muller, C. A., & Tinbergen, J. 1964, BAN, 17, 465
Bernardi, G., de Bruyn, A. G., Brentjens, M. A., et al. 2009, A&A, 500, 965
Bracco, A., Ntormousi, E., Jelić, V., et al. 2022, A&A, 663, A37
Brentjens, M. A., & de Bruyn, A. G. 2005, A&A, 441, 1217
Brouw, W. N., & Spoelstra, T. A. T. 1976, A&AS, 26, 129
Brown, J. C., Taylor, A. R., & Jackel, B. J. 2003, ApJS, 145, 213
Burn, B. J. 1966, MNRAS, 133, 67
Carretti, E., Haverkorn, M., Staveley-Smith, L., et al. 2019, MNRAS, 489, 2330
CHIME & GMIMS collaborations 2024, Faraday tomography with CHIME: the "tadpole" feature G137+7, Canadian Astronomical Data Centre, doi:10.11570/24.0001
CHIME Collaboration 2022, ApJS, 261, 29
CHIME Collaboration 2023, ApJ, 947, 16
CHIME/FRB Collaboration 2021, ApJS, 257, 59
Dickey, J. M., Landecker, T. L., Thomson, A. J. M., et al. 2019, ApJ, 871, 106
Dickey, J. M., West, J., Thomson, A. J. M., et al. 2022, ApJ, 940, 75
Draine, B. 2011, Physics of the Interstellar and Intergalactic Medium (Princeton: Princeton Univ. Press)
Erceg, A., Jelić, V., Haverkorn, M., et al. 2022, A&A, 663, A7
Farnsworth, D., Rudnick, L., & Brown, S. 2011, AJ, 141, 191
Ferrière, K., West, J. L., & Jaffe, T. R. 2021, MNRAS, 507, 4968
Ferrière, K. M. 2001, RvMP, 73, 1031
Foster, T., Kothes, R., & Brown, J. C. 2013, ApJL, 773, L11
Gaensler, B. M., Dickey, J. M., McClure-Griffiths, N. M., et al. 2001, ApJ, 549, 959
Gaia Collaboration, Vallenari, A., Brown, A. G. A., et al. 2023, A&A, 674, A1
Haffner, L. M., Dettmar, R. J., Beckman, J. E., et al. 2009, RvMP, 81, 969
Haffner, L. M., Reynolds, R. J., Madsen, G. J., et al. 2010, in ASP Conf. Ser. 438, The Dynamic Interstellar Medium: A Celebration of the Canadian Galactic Plane Survey, ed. R. Kothes, T. L. Landecker, & A. G. Willis (San Francisco, CA: ASP), 388
Haffner, L. M., Reynolds, R. J., Tufte, S. L., et al. 2003, ApJS, 149, 405
Hausen, N. R., Reynolds, R. J., & Haffner, L. M. 2002, AJ, 124, 3336
Haverkorn, M. 2015, in Magnetic Fields in Diffuse Media, ed. A. Lazarian, E. M. de Gouveia Dal Pino, & C. Melioli (Berlin: Springer), 483
Haverkorn, M., Katgert, P., & de Bruyn, A. G. 2003, A&A, 404, 233
Heald, G. 2009, in IAU Symp. 259, Cosmic Magnetic Fields: From Planets, to Stars and Galaxies, ed. K. G. Strassmeier, A. G. Kosovichev, & J. E. Beckman, 591
Heiles, C. 1967, ApJS, 15, 97
Heiles, C. 2002, in ASP Conf. Ser. 278, Single-Dish Radio Astronomy: Techniques and Applications, ed. S. Stanimirovic et al. (San Francisco, CA: ASP), 131
Heiles, C., & Haverkorn, M. 2012, SSRv, 166, 293
HI4PI Collaboration, Ben Bekhti, N., & Flöer, L. 2016, A&A, 594, A116
Hill, A. S., Benjamin, R. A., Kowal, G., et al. 2008, ApJ, 686, 363
Huang, Y. 2015, IAUGA, 29, 2251816
Hunter, J. D. 2007, CSE, 9, 90
Hutschenreuter, S., Anderson, C. S., Betti, S., et al. 2022, A&A, 657, A43
Iacobelli, M., Haverkorn, M., & Katgert, P. 2013, A&A, 549, A56
IAU 1973, Transactions of the International Astronomical Union, 15, 165
Ideguchi, S., Takahashi, K., Akahori, T., Kumazaki, K., & Ryu, D. 2014, PASJ, 66, 5
Jenkins, E. B. 2013, ApJ, 764, 25
Kothes, R., Sun, X. H., Reich, W., & Foster, T. J. 2014, ApJL, 784, L26
Landecker, T. L., Dewdney, P. E., Burgess, T. A., et al. 2000, A&AS, 145, 509
Landecker, T. L., Reich, W., Reid, R. I., et al. 2010, A&A, 520, A80
Mao, S. A., McClure-Griffiths, N. M., Gaensler, B. M., et al. 2012a, ApJ, 755, 21
Mao, S. A., McClure-Griffiths, N. M., Gaensler, B. M., et al. 2012b, ApJ, 759, 25
Masui, K. W., Shaw, J. R., Ng, C., et al. 2019, ApJ, 879, 16
Mckinven, R., Gaensler, B. M., Michilli, D., et al. 2023, ApJ, 950, 12
Mckinven, R., Michilli, D., Masui, K., et al. 2021, ApJ, 920, 138
OpenAI, 2023 ChatGPT, https://beta.openai.com/chatgpt/
Ordog, A., Brown, J. C., Kothes, R., & Landecker, T. L. 2017, A&A, 603, A15
O'Sullivan, S. P., Brown, S., Robishaw, T., et al. 2012, MNRAS, 421, 3300
Purcell, C. R., Van Eck, C. L., West, J., Sun, X. H., & Gaensler, B. M., 2020 RM-Tools: Rotation measure (RM) synthesis and Stokes QU-fitting, Astrophysics Source Code Library, ascl:2005.003
Ransom, R. R., Kothes, R., Geisbuesch, J., Reich, W., & Landecker, T. L. 2015, ApJ, 799, 198
Ransom, R. R., Kothes, R., Wolleben, M., & Landecker, T. L. 2010, ApJ, 724, 946
Reich, W., Fürst, E., Reich, P., & Reif, K. 1990, A&AS, 85, 633
Reich, W., Fürst, E., Reich, P., et al. 2004, in The Magnetized Interstellar Medium, ed. B. Uyanıker, W. Reich, & R. Wielebinski, 45
Reid, M. J., Menten, K. M., Brunthaler, A., et al. 2014, ApJ, 783, 130
Rudnick, L., & Cotton, W. D. 2023, MNRAS, 522, 1464
Schnitzeler, D. H. F. M., Katgert, P., & de Bruyn, A. G. 2007, A&A, 471, L21
Schnitzeler, D. H. F. M., Katgert, P., & de Bruyn, A. G. 2009, A&A, 494, 611
Soderblom, D. R., Pendleton, J., & Pallavicini, R. 1989, AJ, 97, 539
Sokoloff, D. D., Bykov, A. A., Shukurov, A., et al. 1998, MNRAS, 299, 189
Sun, X. H., Rudnick, L., Akahori, T., et al. 2015, AJ, 149, 60
Tahani, M., Glover, J., Lupypciw, W., et al. 2022a, A&A, 660, L7
Tahani, M., Lupypciw, W., Glover, J., et al. 2022b, A&A, 660, A97
Tahani, M., Plume, R., Brown, J. C., & Kainulainen, J. 2018, A&A, 614, A100
Takahashi, K. 2023, PASJ, 75, S50
Taylor, A. R., Gibson, S. J., Peracaula, M., et al. 2003, AJ, 125, 3145
Taylor, A. R., Stil, J. M., & Sunstrum, C. 2009, ApJ, 702, 1230
Thomson, A. J. M., Landecker, T. L., Dickey, J. M., et al. 2019, MNRAS, 487, 4751
Thomson, A. J. M., Landecker, T. L., McClure-Griffiths, N. M., et al. 2021, MNRAS, 507, 3495
Thomson, A. J. M., McConnell, D., Lenc, E., et al. 2023, PASA, 40, e040
Uyanıker, B., Fürst, E., Reich, W., Reich, P., & Wielebinski, R. 1998, A&AS, 132, 401
Uyanıker, B., Fürst, E., Reich, W., Reich, P., & Wielebinski, R. 1999, A&AS, 138, 31
Uyanıker, B., Landecker, T. L., Gray, A. D., & Kothes, R. 2003, ApJ, 585, 785
Van Eck, C. L., Brown, J. C., Ordog, A., et al. 2021, ApJS, 253, 48
Van Eck, C. L., Haverkorn, M., Alves, M. I. R., et al. 2017, A&A, 597, A98
Van Eck, C. L., Haverkorn, M., Alves, M. I. R., et al. 2019, A&A, 623, A71
Verschuur, G. L. 1968, Obs, 88, 15
Verschuur, G. L. 1969, AJ, 74, 597
West, J. L., English, J., Normandeau, M., & Landecker, T. L. 2007, ApJ, 656, 914
Westerhout, G., Brouw, W. N., Muller, C. A., & Tinbergen, J. 1962, AJ, 67, 590
Wielebinski, R., Shakeshaft, J. R., & Pauliny-Toth, I. I. K. 1962, Obs, 82, 158
Wolfire, M. G., McKee, C. F., Hollenbach, D., & Tielens, A. G. G. M. 2003, ApJ, 587, 278
Wolleben, M., Landecker, T. L., Carretti, E., et al. 2019, AJ, 158, 44
Wolleben, M., Landecker, T. L., Douglas, K. A., et al. 2021, AJ, 162, 35
Wolleben, M., Landecker, T. L., Reich, W., & Wielebinski, R. 2006, A&A, 448, 411